Review

X-ray magnetic circular dichroism—a high energy probe of magnetic properties

Tobias Funk [b], Aniruddha Deb [c], Simon J. George [b,*], Hongxin Wang [b], Stephen P. Cramer [b,a]

[a] *Department of Applied Science, University of California, Davis, California 95616, USA*
[b] *Physical Biosciences Division, Lawrence Berkeley National Laboratory, Berkeley, California 94720, USA*
[c] *Environmental Energy Technologies Division, Lawrence Berkeley National Laboratory, Berkeley, California 94720, USA*

Contents

* Corresponding author. Tel.: +1 510 486 6094; fax: +1 510 486 5664.
E-mail address: SJGeorge@lbl.gov (S.J. George).

Abstract

X-ray magnetic circular dichroism (XMCD) spectroscopy is a powerful emerging technique that measures difference in absorption of left- and right-circularly polarized X-rays by a magnetized sample, often at cryogenic temperatures. It is already well established in magnetic materials science, and it is likely to become a significant tool for the inorganic and bioinorganic communities. As with all X-ray spectroscopies, XMCD has the advantage of being element specific. Interpretation of the spectra can: provide quantitative information about the distribution of spin and orbital angular momenta from simple "sum rules"; determine spin orientations from the sign of the XMCD signal; infer spin states from magnetization curves; and separate magnetic and non-magnetic components in heterogeneous samples. With new synchrotron radiation sources and improved end stations, XMCD measurements on dilute samples such as metals in enzymes, are becoming more routine. This review first details the technology currently available for XMCD measurements and outlines the theory underlying interpretation of the spectra. It then illustrates the strengths of the XMCD technique using examples taken from bioinorganic chemistry and materials science. In this way, we aim to encourage chemists, materials scientists, and biologists to consider XMCD spectroscopy as an approach to understanding the electronic and magnetic structure of their samples.
© 2004 Elsevier B.V. All rights reserved.

1. Introduction

1.1. The XMCD effect

X-ray magnetic circular dichroism (XMCD) is the difference in absorption of left- and right-circularly polarized X-rays by a magnetized sample (Fig. 1) [1]. Although MCD with X-rays is only about 15 years old, the physics is essentially the same as for the UV–vis MCD that has been known since 1897 [2]. For (bio)inorganic chemists and materials scientists, XMCD has the advantage of elemental specificity that comes with all core electron spectroscopies. Thanks to simple sum rules, XMCD can also provide quantitative information about the distribution of spin and orbital angular momenta. Other strengths include the capacity to determine spin orientations from the sign of the XMCD signal, to infer spin states from magnetization curves, and the ability to separate magnetic and non-magnetic components in hetero-

geneous samples. With new synchrotron radiation sources and improved end stations, XMCD measurements on biological samples are, if not routine, at least no longer heroic. One goal of this review is to encourage chemists, materials scientists, and biologists to consider XMCD as an approach to understanding the electronic and magnetic structure of their samples.

1.2. Circular polarization

A circularly polarized X-ray has oscillating electric and magnetic fields that are $90°$ out of phase with each other. We use the convention of Born and Wolfe [3], in which the instantaneous electric field $\vec{E}_{rcp}$ for a right circularly polarized photon propagating in the z-direction resembles a right-handed screw (Fig. 1).

$$\vec{E}_{rcp} = E_0\{\sin[\omega t - kz + \phi_0]\boldsymbol{i} + \cos[\omega t - kz + \phi_0]\boldsymbol{j}\} \quad (1)$$
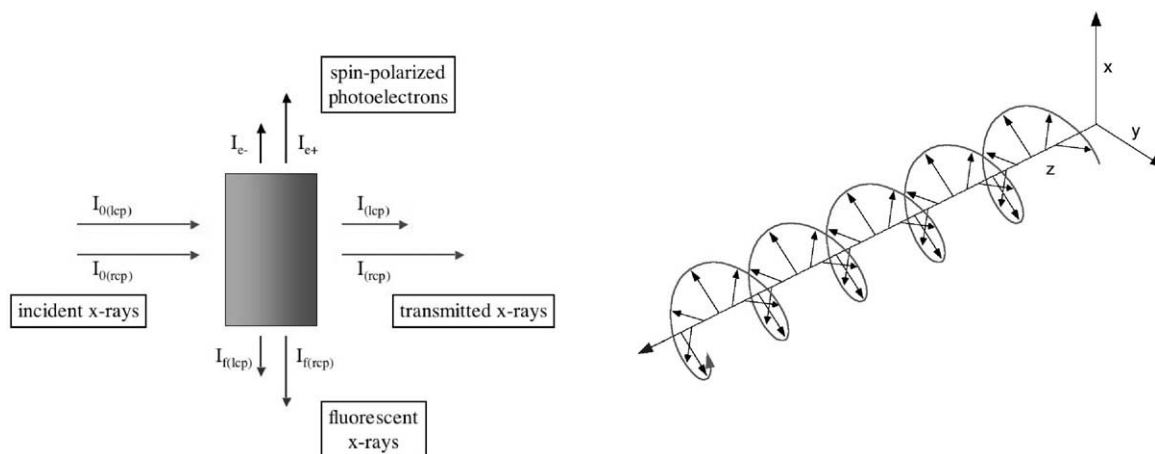

Fig. 1. (Left) Schematic of XMCD experiment. I_0 is incident beam intensity, I is the transmitted intensity while I_f and I_e are the intensities of the emitted fluorescence and photoelectrons respectively. (Right) Illustration of the electric field direction along the propagation axis for right circularly polarized light.
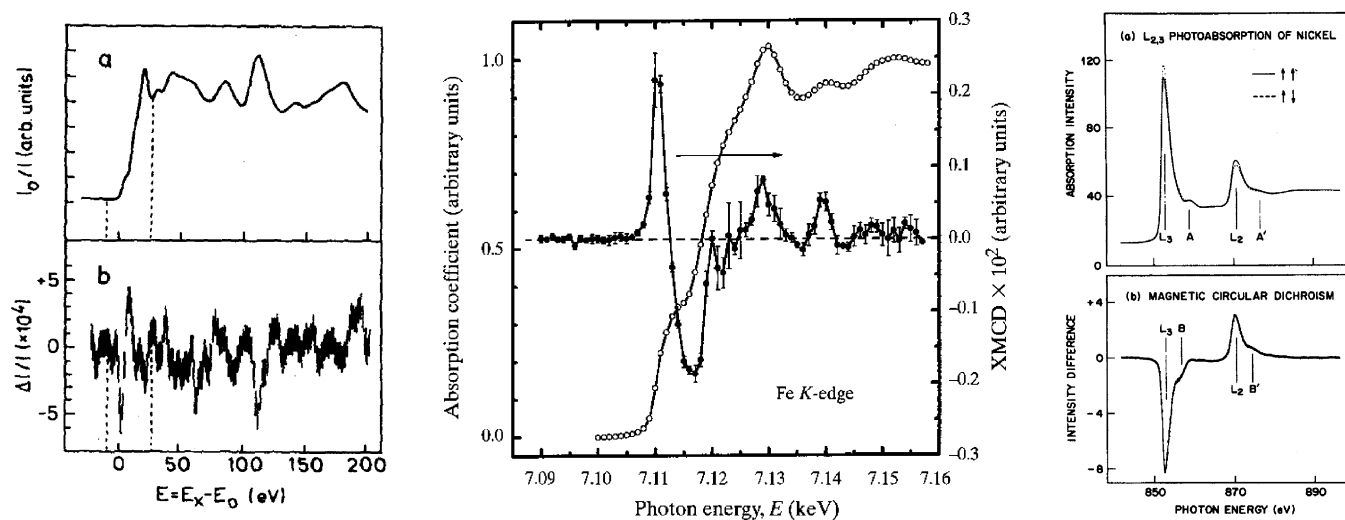
Fig. 2. (Left) First Fe K-edge XANES and EXAFS (different scales) XMCD spectra. Reprinted with permission from [22]. Copyright (1987), American Physical Society. (Middle) More recent Fe XMCD from the APS. (Right) First soft X-ray MCD spectrum, reported for Ni metal. Reprinted with permission from [23]. Copyright (1990), American Physical Society.

In this equation, ω is the angular frequency, $\omega = 2\pi\nu$, k is the wave number, $k = 2\pi/\lambda$, where λ is the wavelength, ϕ_0 is an arbitrary phase shift, and i and j are unit vectors along the x and y axes, respectively. With the above definition, it turns out that left circularly polarized photons carry $\hbar$ angular momentum. Beth [4] observed the predicted torque on a macroscopic target in a torsion pendulum experiment in 1936.

Although the Born and Wolf convention is standard for optics and chemistry literature, most physics literature uses the opposite definition, and one should check how the polarization is defined if the sign of the MCD effect is to be meaningful. The papers of deGroot and Brouder generally use the Born and Wolfe convention, while those of Thole, van der Laan, and Carra use the physics or 'Feynman' definition [5]. The pitfalls of describing circular polarization have been cogently described by Kliger et al. [6].

1.3. Some history

The existence of polarized light has been known since at least 1690, when Huygens [7] discovered that either of the two light rays refracted by a calcite crystal could be extinguished by rotation of a second 'analyzer' crystal. More than a century later (1808), Maulus observed that sunlight reflected from a window pane had similar properties, and by analogy with magnetic bodies, he called this light 'polarized' [8]. Although these early observations were first interpreted in terms of Newton's 'corpuscular' theory [9], by the 1820s Fresnel had developed a mathematical description for polarized light in terms of two perpendicular transverse waves [10]. In 1846, Faraday demonstrated rotation of the plane of polarization induced by a magnetic field [11,12]; this 'Faraday effect' or 'magnetic optical rotation' is the result of circular birefringence—a difference in the real part of the complex index of refraction $\tilde{n}$ for left and right circular polarization. Prompted in part by these results, the theoretical work of Maxwell completed the picture of light as an electromagnetic wave [13].

The first demonstration of a magnetically induced difference in absorption (the imaginary part of $\tilde{n}$) came with the Nobel prize-winning work of Zeeman. After first observing both linear and magnetic circular dichroism in the sodium D emission lines in a magnetic field [14], he reversed the experiment and observed MCD effects on the D absorption lines of Na vapor [2].

Shortly after the discovery of X-rays by Röntgen in 1895 [15], attempts were made to observe magnetic effects on X-ray spectra [16,17]. However, a successful experiment would have to wait another 80 years. The modern history of XMCD begins with Erskine and Stern [18] predicting a magneto-optical Kerr effect (MOKE) for ferromagnetic Ni at the $M_{2,3}$-edge (3p → 3d). Subsequent attempts to see XMCD in a GdFe alloy at the Gd L_3-edge were unsuccessful [19]. A year later, Thole et al. [20] predicted strong XMCD and X-ray magnetic linear dichroism (XMLD) in the $M_{4,5}$ (3d → 4f)-edges of rare-earths, and the latter was reported in 1986 [21]. The XMCD effect was finally observed at the K-edge of metallic Fe by Schütz et al. [22] in 1987 (Fig. 2). A much stronger soft X-ray MCD at the Ni $L_{2,3}$-edge was reported in 1990 (Fig. 2) [23]. Our group reported the first XMCD for a paramagnetic metalloprotein in 1993 [24]. Since then, the growth of XMCD for materials science applications has been explosive [25], leading to more than 1000 papers over the past decade.

2. Experimental considerations

Key ingredients for an XMCD measurement are: (1) a source of circularly polarized X-rays, (2) a monochromator and optics (a 'beamline'), (3) a means for producing a

magnetized sample, and (4) an X-ray absorption detection system. The latter two are considered the 'endstation'.

2.1. Sources of circularly polarized X-rays

Before the introduction of synchrotron radiation facilities, sources of circularly polarized high energy photons were exotic, such as magnetically oriented radioactive nuclei [26,27] and astronomical synchrotron radiation [28]. Although the concepts behind X-ray circular polarizers had been demonstrated with Cu Kα radiation [29], the resultant beams were not bright enough (∼15 photons/s) for practical applications. The frustration of pre-synchrotron X-ray physicists can be heard in the comments of Skalicky and Malgrange, "*in principle therefore all polarization experiments which are possible with visible light can be performed with X-rays (but) . . . it is in practice difficult to obtain sufficient intensity [30]*".

2.1.1. Bend magnets

The bend magnets associated with particle storage rings are the simplest sources of circular polarization. By viewing the particle beam off-axis, one observes a charge accelerated in an elliptical orbit, while viewing the beam on-axis reveals

only a horizontal component to the acceleration (Fig. 3). Thus, the synchrotron radiation emitted from bend magnets is highly polarized—ranging from pure linear polarization in the plane of the orbit to nearly circular far out of the plane. Borrowing from Kim [31], the relative amplitudes of the horizontal and vertical electric field components (E_x and E_y) are given by (Fig. 3):

$$\begin{pmatrix} E_x \\ E_y \end{pmatrix} = \begin{pmatrix} K_{2/3}(\eta) \\ \dfrac{i\gamma\psi K_{1/3}(\eta)}{\sqrt{1 + (\gamma\psi)^2}} \end{pmatrix} \qquad (2)$$

where $K_{1/3}$ and $K_{2/3}$ are modified Bessel functions, y is the ratio of photon energy to the critical energy, γ is the ratio of the electron energy to its rest mass energy, and $\eta = (y/2) [1 + (\gamma y)^2]^{3/2}$. Defining r as the ratio of the minor to major axes of the polarization ellipse, given by $r = E_y/iE_x$, yields the degree of circular polarization P_c (defined as P_3 by Kim): $P_c = 2r/(1 + r^2)$ [31].

Although bend magnets can provide any desired degree of polarization, this comes at a price—the flux falls dramatically as ψ increases. The strongest XMCD is obtained with
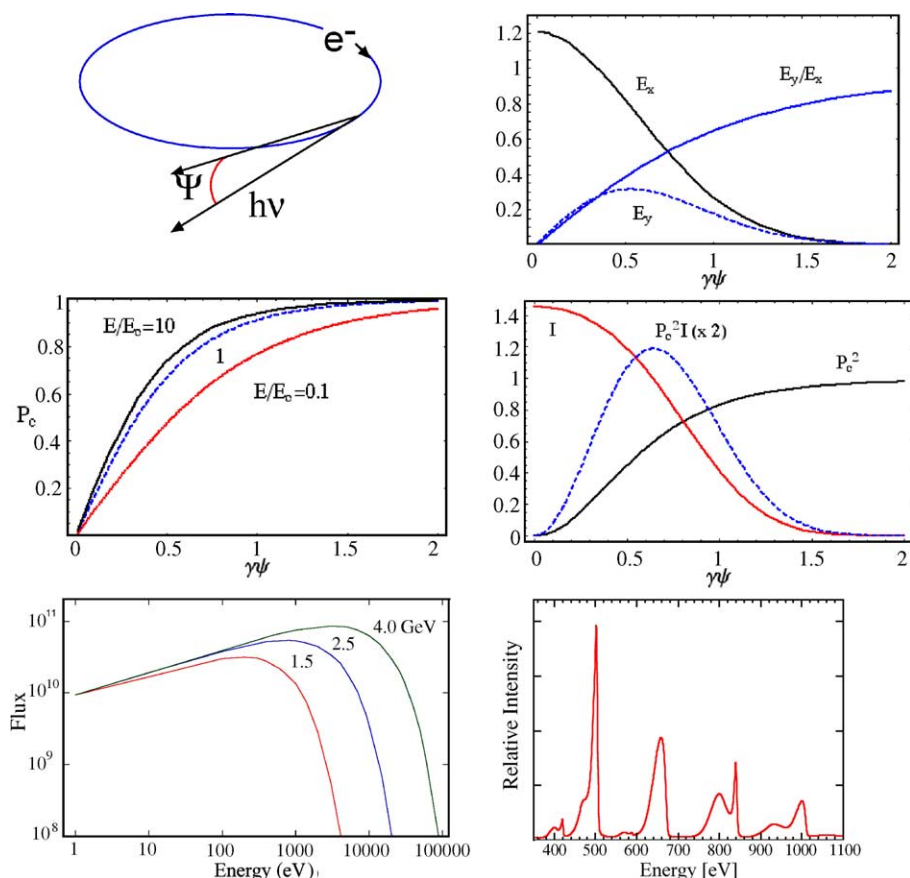
Fig. 3. (Top left) Definition of observation angle ψ for synchrotron radiation with respect to the orbital plane. (Top right) Amplitudes of *x*- and *y*-components of the electric field vs. $\gamma\psi$. (Middle left) Degree of circular polarization P_c as a function of the vertical viewing angle ψ. E/E_c is the X-ray energy divided by the storage ring's critical energy. (Middle right) Tradeoff between flux and polarization, and the figure of merit $P_c^2 I$ (Bottom left) Calculated brightness spectrum for a bend magnet at different ring energies. (Bottom right) Measured output of the ALS EPU.

pure circular polarization, but as $P_c \to 1$, $I \to 0$. One therefore has to make a tradeoff between flux and polarization. A figure of merit for most XMCD experiments is $P_c^2 I$, and the angle for optimal $P_c^2 I$ depends on the photon energy and the critical energy of the ring (Fig. 3). Apart from limited P_c, other drawbacks of bend magnets are modest brightness and the emission of lcp and rcp in different directions. Better XMCD measurements can be done with insertion device beamlines.

2.1.2. Insertion devices

Insertion devices are magnetic structures 'inserted' into straight sections of a storage ring lattice to produce synchrotron radiation with special characteristics. Table 1 lists a variety of the insertion device beamlines available at synchrotron facilities worldwide. One clever approach proposed by Goulon et al. [32] and others [33] is the 'asymmetric wiggler'. In this device, a strong magnetic field bends the charged particle sharply in one direction, and subsequently a pair of weaker magnetic regions brings the particle back in the opposite direction (Fig. 4). The result is an emission pattern with strong circular polarization at high energies. In the related 'elliptical wiggler' [34], the field is arranged to produce an orbit that spirals around the central axis in an elliptical manner (Fig. 4). This source can be considered as an array of tilted bend magnets arranged to produce the same polarization along the wiggler axis. Other devices, such as helical undulators and crossed undulators (Fig. 4) are also in use [35,36].

The elliptical undulator (EPU) is one of the most successful devices for the production of circularly polarized synchrotron radiation. In an EPU, the magnetic field vector rotates as a particle passes through the device, causing the particle to spiral about a central axis. Both electromagnetic and permanent magnet versions have been developed (Fig. 4). Permanent magnet EPUs consist of four banks of magnets—two on top and two below (Fig. 4). The peak energy of the undulator output is changed by varying the vertical separation between the magnet assemblies, a so-called 'gap scan', while the polarization is varied by changing the relative positions (phases) of adjacent rows of magnets—a 'row scan'. In the case of the EPU on ALS beamline 4.0.2, the polarization can be changed from left to right circular polarization in a few seconds, and the peak energy can be varied as quickly as the monochromator scans [37].

2.1.3. Soft X-ray beamlines

In the soft X-ray region, beamlines use grazing incidence mirrors and gratings. In these geometries, the source polarization is almost completely preserved as it passes through the optics. For example, ALS beamline 4.0.2 employs an initial horizontally deflecting toroid (M1) at $2°$, a plane pre-mirror (M3) at $\sim 3°$, a plane grating at variable glancing angle, a cylindrical magnifying mirror (M4) at $\sim 1°$, and a final refocusing mirror (M5) at $\sim 1°$ (Fig. 5). This beamline provides $\sim 10^{12}$ photons/s between 50 and 2000 eV with $\Delta E/E \sim 20,000$ at the lower energy [37].

2.1.4. Hard X-ray beamlines and quarter wave plates

Hard X-ray applications could employ the same sources of circular polarization, but crystal monochromators are generally used in this region, and the effect of the crystal optics on the beam polarization can be considerable. A well-known property for visible light reflection is the so-called 'Brewster angle'—the angle of incidence at which the electric field in the plane of incidence (π component) of a reflected beam is totally suppressed. This results in pure linear polarization along the out-of-plane or σ direction. The same phenomenon can occur with Bragg reflection from crystals. Despite

Table 1
Partial list of worldwide synchrotron XMCD facilities

Storage ring facility	Beamline	CP X-ray source	Energy range	Endstation(s) magnet/cryostat
ALS, Berkeley, CA, USA	4.0.2	EPU	50–1900 eV	6 T, 0.5 K 2 T, 0.1 K
APS, Argonne, IL, USA	4-ID-D	Undulator with phase retarder	3–50 keV	
	4-ID-C	EPU	0.5–2.8 keV	
DELTA, Dortmund, Germany		Superconducting AW	$\sim$3–22 keV	
ESRF, Grenoble, France	ID08	Twin EPU	0.5–1.6 keV	7 T, 1.5 K
	ID12A	Twin HU	3–22 keV	7 T, 1.5 K
ELETTRA, Trieste, Italy	8.2 (BACH)	Twin EPU	0.35–1.6 keV	7 T, 77 K
LURE/ACO, Orsay, France	SU 23	AW	100–1000 eV	7 T, 20 K
NSLS II, Upton, NY, USA	U4B	Bend magnet	20–1200 eV	5 T
SPring-8, Hyogo, Japan	BL08W	EW	70–300 keV	3 T, 10 K
	BL25SU	Twin HU	0.22–2 keV	1.4 T permanent
	BL39XU	Undulator with phase retarder	5–37 keV	10 T, 1.7 K
SRS, Daresbury, UK	1.1	Bend magnet	200–1000 eV	5 T, 1.6 K
SSRL, Stanford, USA	8-2	Bend magnet	80–1200 eV	
	5-2	EPU	10–1200 eV	

AW: asymmetric wiggler; HU: helical undulator; EW: elliptical wiggler; EPU: elliptically polarizing undulator.
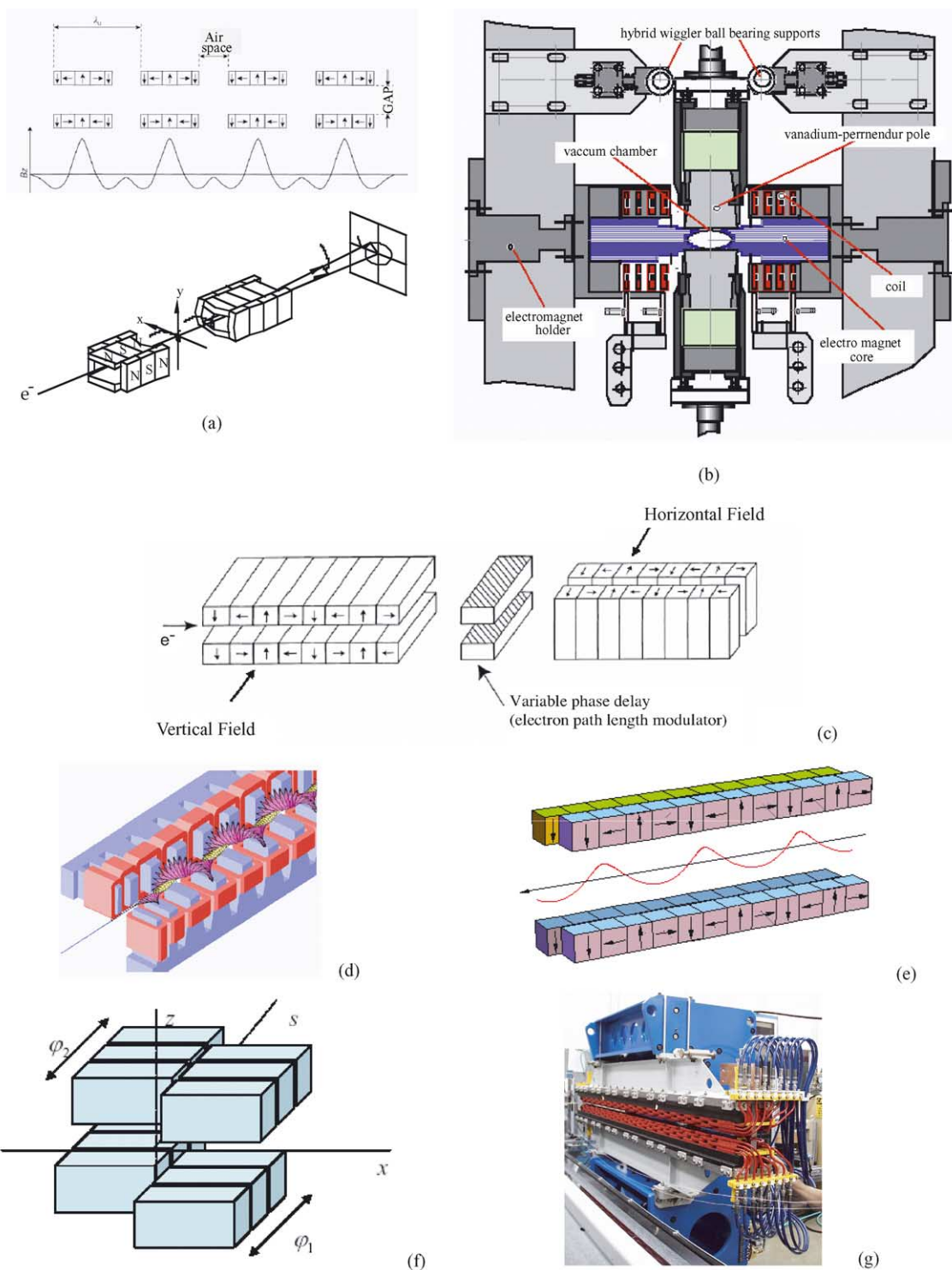
Fig. 4. (a) Magnetic field profile in an AW. (b) Magnetic assembly and particle orbit in an EW. (c) Concept for circular polarization from two crossed undulators. (d) Magnets and particle path in an HU. (e) Magnets and particle path in an EPU. (f) Sliding magnet assemblies in an EPU. (g) An electromagnetic polarizing undulator at the APS [44].

perfect circular polarization from a hard X-ray EPU, the crystal optics could degrade the degree of circular polarization and in some cases produce pure horizontal polarization! (For X-rays the Brewster angle is close to 45°, and for diffraction near normal or glancing incidence, the loss of circular polarization is not significant.)

The solution is the same approach used with UV–vis MCD experiments—start with linear polarization and
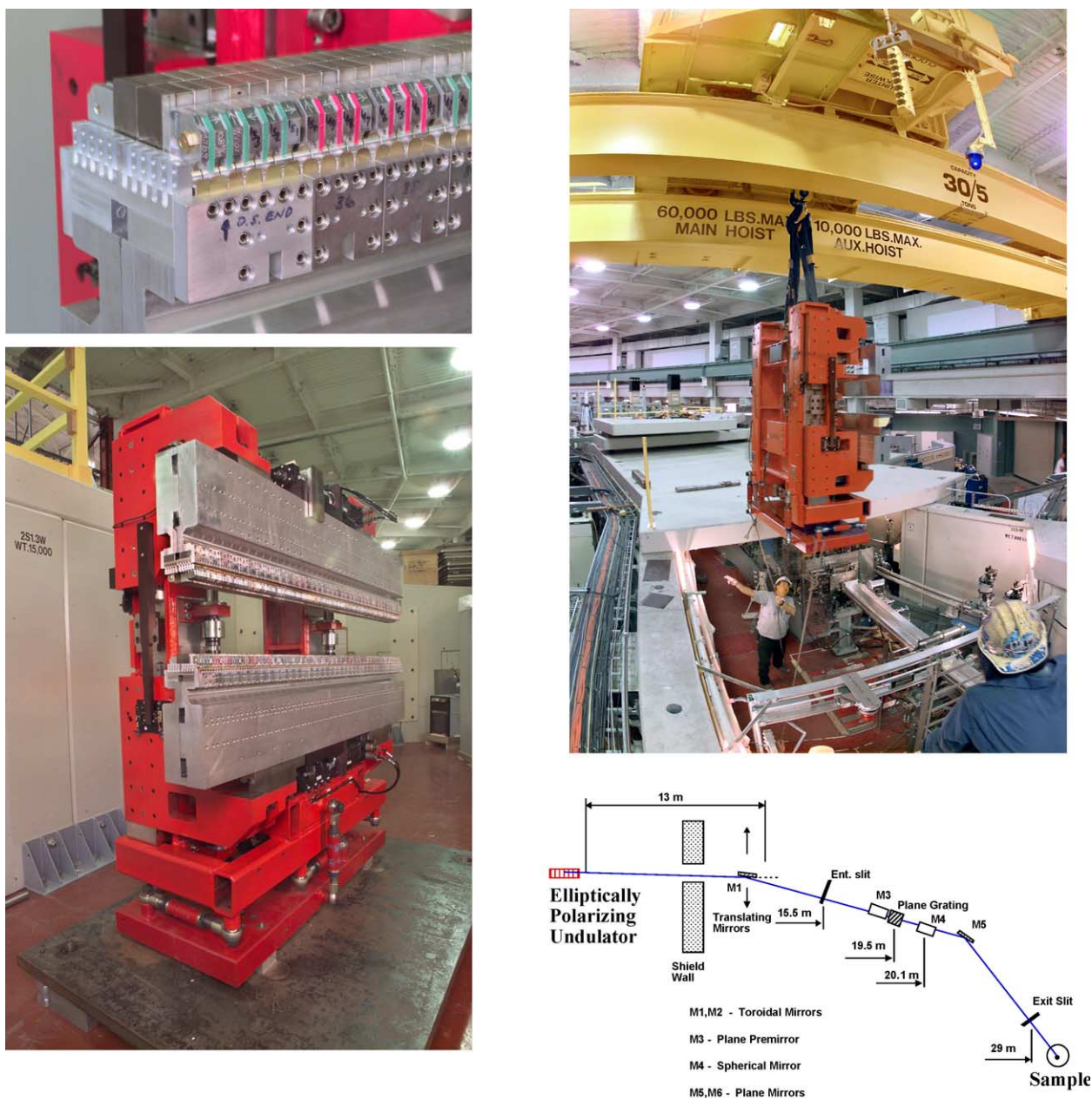
Fig. 5. Photographs of the ALS EPU. (Top left) A section of the bottom pair of magnet quadrants in the ALS EPU. Each period (e.g. "35" and "36") is 5 cm long. (Bottom left) The entire EPU assembly. (Top right) Installation of the EPU into the ALS ring. The jaws will wrap around the Al beam pipe at lower right. (Bottom right) Schematic of the ALS EPU beamline.

convert to circular polarization with a retarder, commonly a quarter wave plate. X-ray quarter wave plates exploit the birefringence of crystals for σ and π electric field components for geometries on or close to diffraction conditions. Although early work emphasized on-reflection Bragg or Laue geometries [29,30,38–40], the most popular X-ray quarter wave plates operate in the off-Bragg transmission geometry. In this case, the crystal is adjusted to one of the wings of the Bragg reflection, at an angular deviation $\Delta\theta$ from the center of the rocking curve for Bragg angle θ_B. The crystal planes are placed at a $45°$ angle to the incident polarization direction, to allow equal intensity for σ and π

components of the electric field. The phase shift $\Delta\phi$, for a sufficiently large $\Delta\theta$, depends on the difference in indices of refraction ($n_\sigma - n_\pi$), as well as the beam path t and wavelength λ, and is given by [41]:

$$\Delta\phi = \frac{2\pi}{\lambda}(n_\sigma - n_\pi)t$$
$$= -\left[\frac{r_e{}^2 F_h F_{\bar{h}}}{2\pi V^2}\frac{\lambda^3 \sin 2\theta_B}{\Delta\theta}\right]t = A\frac{t}{\Delta\theta} \quad (3)$$

F_h and $F_{\bar{h}}$ are structure factors for h and $\bar{h}$ reflections, r_e is the classical electron radius, and V is the unit cell volume.
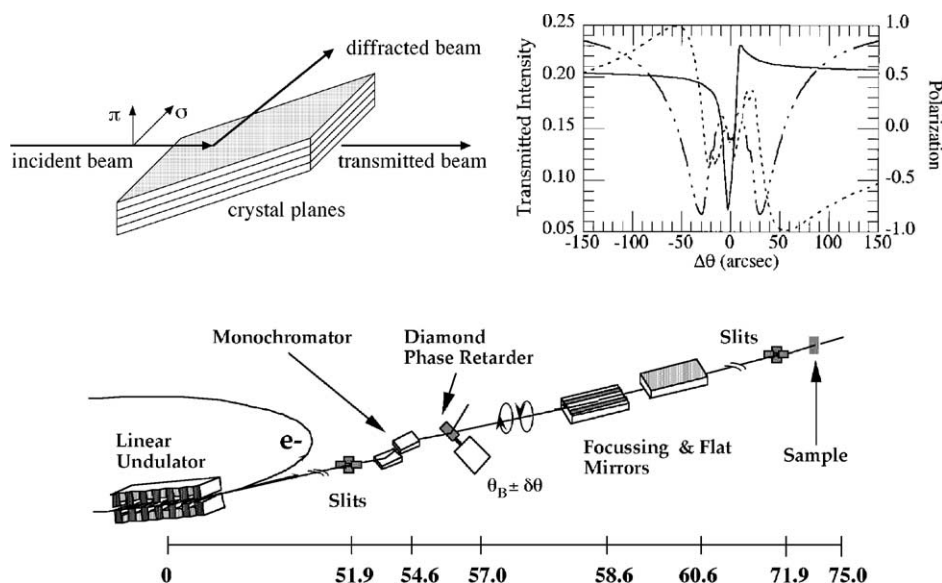
Fig. 6. (Top left) Bragg reflection and transmission geometries for X-ray quarter wave plates. (Top right) Phase shift difference for σ and π components as a function of the offset ($\Delta\theta$) from the Bragg condition. (Bottom) APS 4-ID-D, a hard X-ray beamline that employs quarter wave plates to provide circularly polarized X-rays. Reprinted with permission from [44]. Copyright (2002), American Institute of Physics.

By rocking a low-Z crystal such as diamond [42], Be [41], or LiF [43], from one side of the Bragg reflection to another, the polarization can be switched from lcp to rcp, with a P_c > 90%. APS 4-ID-D is one beamline that uses such quarter wave plates (Fig. 6) [44].

2.2. Magnetic field and temperature control

The simplest samples for XMCD experiments are permanent magnets, such as the domains in disk storage devices. These samples can be magnetized separately from the XMCD measurement. For example, Stöhr et al. [45] have used the XMCD effect to image magnetic domains in disk storage devices. Other groups have magnetized thin film samples in situ with a pulsed magnetic field, which is then turned off during the experiment [46,47]. Ferromagnets are also easy to study, since only a small field need be applied. For example, the early measurements of Chen and co-workers used an external cylindrical permanent magnet in close proximity to the Ni foil. The field was switched by manually reversing the external magnet [23]. NdFeB alloy permanent magnets are still used in some experiments to polarize the sample. Electromagnets make this process easier to automate, and several groups have used them in a variety of ways [48]. For example, Arenholz has recently built an eight-pole system that, in combination with a sample manipulator that allows 180° polar and 360° azimuthal rotation of the sample, permits any geometry of magnetic field, sample surface, and incident photon direction (Fig. 7).

Superconducting magnets are required to achieve the highest magnetic fields. Our group employs two different split coil designs. In one instrument, a 6 T split coil is used, with a transverse gap between the coils [24,49]. This device has the advantage that full magnetization of the sample is

achieved at 2–3 K, which is readily achieved with pumped ^{4}He cryostats. A temperature of $\sim$0.5 K can be reached by using a ^{3}He insert (Fig. 7) [50]. It has two limitations. First, the small gap limits the size of the Ge detector that can be introduced between the coils; hence we lose some solid angle of fluorescence collection. More important, the relatively large (31 H) inductance limits the rate at which the magnetic field can be reversed. However, because of its relative ease of use, this machine remains the workhorse of our XMCD measurements.

Another, more recent, instrument employs a ^{3}He–^{4}He dilution refrigerator, a split-coil 2 T superconducting magnet system, and a 30-element windowless Ge fluorescence detector [51]. This device has a larger gap (8.25 cm), allowing insertion of the 30-element Ge detector close to the sample. It also has a low inductance winding (1.3 H), allowing field sweeps from + 2 T to −2 T in $\sim$10 s. Several layers of thermal shielding allow temperatures below 0.5 K to be reached routinely (Fig. 7); in principle, 0.1 K should be possible.

2.3. Detection methods

Since XMCD is essentially a measurement of relative absorption coefficients, all of the methods used for conventional XAS can in principle be applied (Fig. 1). In practice, the three most important modes are transmission, fluorescence, and electron yield. As discussed long ago by Lee et al. [52], the preferred mode depends on the concentration and spatial distribution of the element under investigation, as well as the fluorescence yield and the matrix absorption coefficient. Since all of the factors involved in optimizing hard X-ray absorption measurements are well known, we will concentrate on the special requirements for MCD with soft X-rays.
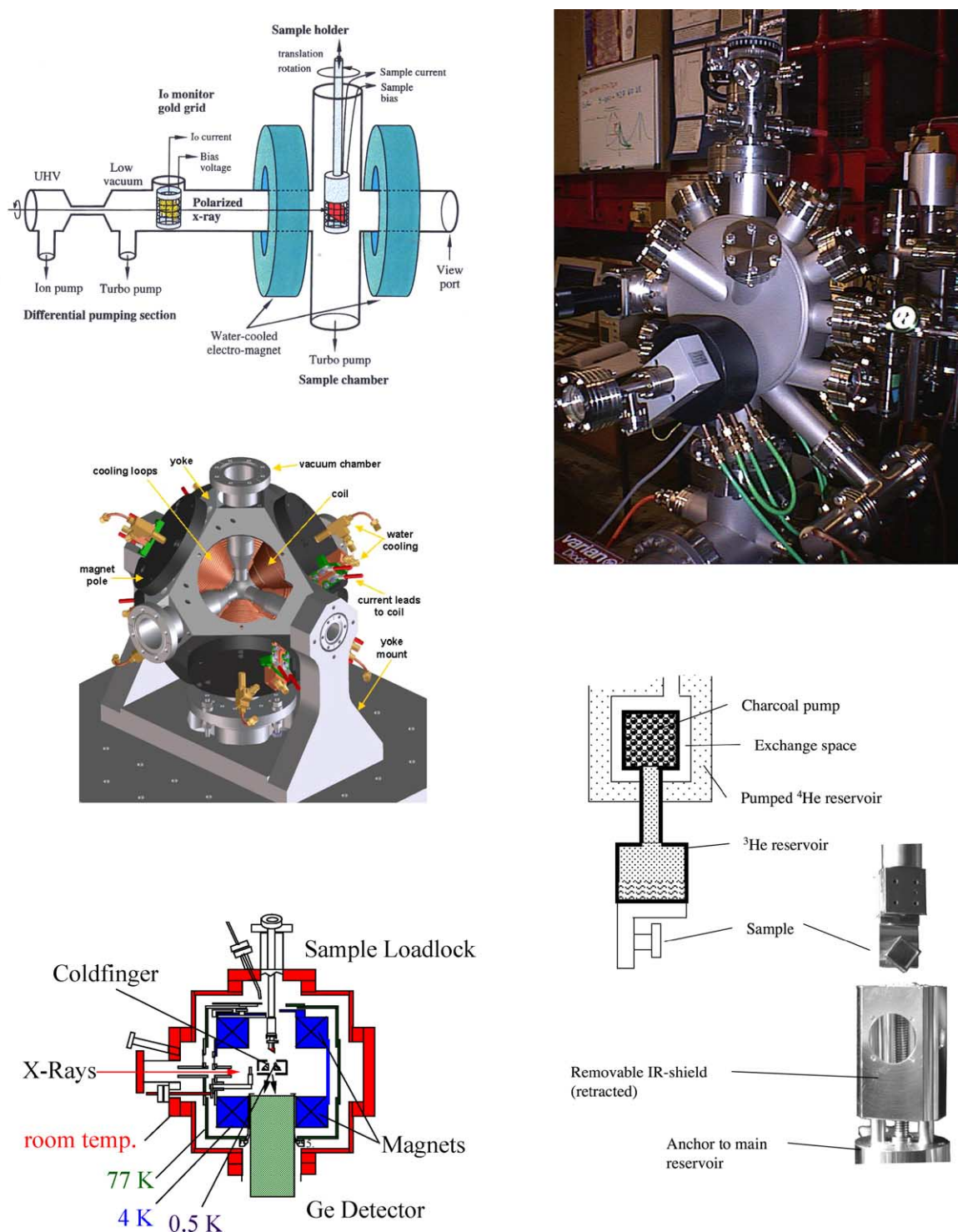
Fig. 7. (Top left) A water-cooled electromagnet XMCD system for electron yield detection employed by Stöhr and coworkers [56]. (Center left) Schematic view of a 'vector magnetometer' developed by Arenholz. (Bottom left) Schematic of the dilution fridge XMCD instrument. (Top right) Photograph of 'Flipper' water-cooled electromagnet XMCD system developed by van der Laan group. (Bottom right) A schematic and photograph of the ^{3}He cryostat from the ALS 6 T, 0.5 K XMCD chamber with its 4.2 K infrared shield.

2.3.1. Transmission

Transmission is the simplest measurement, and it should be used whenever possible. The beam intensity before the sample (I_0) is often measured using the electron yield or photocurrent from a partially transmitting metal grid. The intensity after the sample (I) can be measured using a second grid, a solid metal plate, or a Si photodiode. Chen and coworkers have done careful transmission measurements

of the XMCD of thin metal foils to check the accuracy of the sum rules [53], and with these samples transmission works beautifully. Unfortunately, in the soft X-ray region it is difficult to prepare coordination complexes as homogeneous, pinhole-free samples with the required sub-micron thickness. As discussed by Stern and Kim [54] and Goulon et al. [55], thick or porous samples will have suppressed absorption features due to 'leakage' effects, and consequently diminished XMCD amplitudes, especially if harmonics are present in the incident beam. Since the particle size of most samples is often greater than the $1/e$ (<1 μm) pathlength, diluting the sample in a low-Z powder or mull is of no use.

2.3.2. Electron yield

For concentrated inorganic samples, electron-based detection methods are preferred. One can either measure the electron yield directly with a channeltron electron multiplier (CEM), or indirectly as the 'photocurrent' of electrons flowing to the sample from ground. Since electrons are only emitted from approximately the first 25–50 Å of a sample, these approaches are very sensitive to oxidation or other surface reactivity. For very high cross sections, they can also suffer from saturation effects [56]. A problem for inorganic chemists is that many coordination complexes are poor conductors at the ~ 4 K temperature required for XMCD of paramagnets. To some extent, this can be overcome by: (1) making very thin samples, (2) using a high collection voltage, (3) embedding the sample in a metallic grid, (4) pressing the sample particles into an indium foil, or (5) mixing the sample with a good conductor (Ag or graphite dust). The one generalization we can make from past experience is that every sample is different.

Apart from S/N issues, electron methods may suffer from artifacts if magnetic field switching is used to measure the XMCD effect. The trajectories of emitted photoelectrons will depend not only on their initial velocity, the applied voltage, and the geometry of the collector placement, but also on the magnetic field. The apparent absorption cross section will vary if changing the field affects the fraction of photoelectrons that are accepted. Thus, electron-based XMCD measurements are best done with variable photon polarization.

2.3.3. Fluorescence yield

Fluorescence yield might seem immune from magnetic field artifacts, since the magnetic field will not affect the photons once emitted. However, most detectors convert X-rays into electrons, hence the detector resolution or gain can be influenced by a strong field. The potential detector sensitivity needs to be checked before varying the magnetic field for XMCD measurements or magnetization curves. As pointed out by de Groot et al. [57,58] and others [59], the fluorescence-detected excitation spectrum is not necessarily the same as the absorption spectrum, because the fluorescence yield can vary for different excited states. In extreme cases, a line can even be missing from the excitation spectrum (Fig. 8) [59] ! However, as noted by van Veenendaal et al. [60,61], the effect is not usually that severe for XMCD. They point out that, 'although in principle fluorescence yield is unequal to X-ray absorption, in the presence of a crystal field or of strong core-hole spin-orbit coupling fluorescence yield can be used to obtain ground state expectation values of L_z and S'_z (vide infra) [60]. It is presumably even less important for magnetization curves, where one only needs proportionality at a single point in the spectrum. From an experimentalist's point of view, a fluorescence-detected spectrum with known limitations is better than no spectrum at all.

Finally, it should be noted that even polarization-switched measurements suffer from potential artifacts. If the effective source point for left- and right-circularly polarized beams is slightly different, this can transform into an energy difference between the two beams at a given monochromator position. The slight mismatch will result in a derivative shaped contribution to the spectrum that is stronger for sharper features. Since this effect is independent of the applied field, one should check that there is indeed no XMCD effect in the absence of sample magnetization. (This presumes there is no 'natural' CD effect, but that is another story [62,63].)
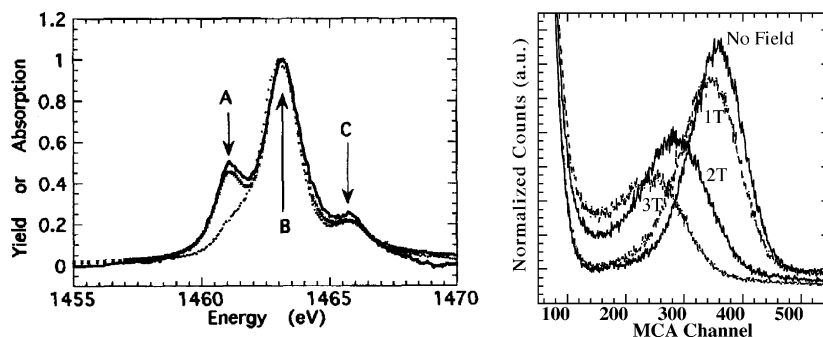

Fig. 8. (Left) An unfavorable case for fluorescence detection. Comparison of transmission (solid line), electron yield (crosses), and fluorescence-detected (dots) absorption spectra for a thin film of Tm. Reprinted with permission from [59]. Copyright (1997), American Physical Society. (Right) Magnetic field effects on Ge fluorescence detector resolution.

3. Simplified theory

A full description of the XMCD effect for a transition metal complex with multiple d-vacancies requires a sophisticated computer program, and even then, the models are only approximations. A simple approach, the 'one-electron picture', is commonly applied to metallic samples, while the more complex 'ligand field multiplet approach' includes Coulomb and exchange integrals and is more often used for transition metal complexes. Below we compare the predictions of both pictures. It should be noted that the ligand field multiplet model reduces to the one-electron approach in the limit where the Coulomb and exchange integrals are zero.

3.1. One-electron theory

A large fraction of the XMCD literature, especially papers involving magnetic thin film and metallic samples, uses the one-electron model along with a two-step approach to XMCD [64]. In this picture, the first step is to write the initial orbitals for first transition metal L-edges as spin-orbit split 2p wave functions, as summarized in Table 2 [64].

The next step is to find expressions for the cross section matrix elements for transitions to various states with d symmetry. Stöhr and Wu [64] write these, citing Bethe and Salpeter [65], as:

$$\left\langle n', l+1, m_l+1 | P_1^{(1)} | n, l, m_l \right\rangle$$
$$= \sqrt{\frac{(l+m_l+2)(l+m_l+1)}{2(2l+3)(2l+1)}} R \tag{4}$$

and

$$\left\langle n', l+1, m_l-1 | P_{-1}^{(1)} | n, l, m_l \right\rangle$$
$$= \sqrt{\frac{(l-m_l+2)(l-m_l+1)}{2(2l+3)(2l+1)}} R \tag{5}$$

where

$$P_1^{(1)} = \frac{1}{\sqrt{2}}(x+iy) = r\sqrt{\frac{4\pi}{3}} Y_1^1 \quad \text{and}$$
$$P_{-1}^{(1)} = \frac{1}{\sqrt{2}}(x-iy) = r\sqrt{\frac{4\pi}{3}} Y_1^{-1} \tag{6}$$

Table 2
Wave functions used in one-electron model

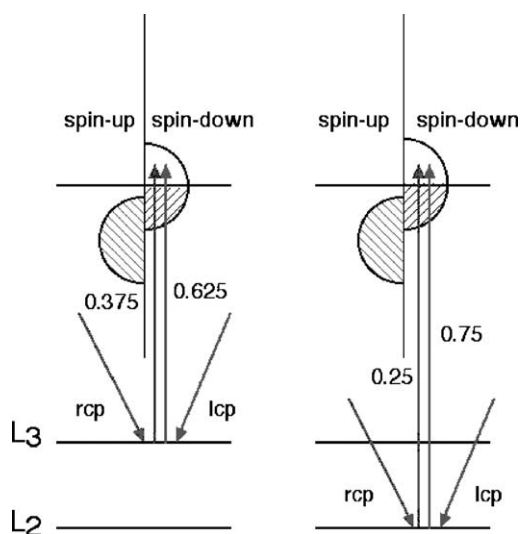| One-electron label	$|1s\, j\, mj\rangle$ basis: m_j	$Y_l^{m_l} \Phi_{ms}$
$P_{1/2}$	1/2	$\frac{1}{\sqrt{3}}(Y_1^0 \alpha - \sqrt{2} Y_1^1 \beta)$
	−1/2	$\frac{1}{\sqrt{3}}(\sqrt{2} Y_1^{-1} \alpha - Y_1^0 \beta)$
$P_{3/2}$	3/2	$Y_1^1 \alpha$
	1/2	$\frac{1}{\sqrt{3}}(\sqrt{2} Y_1^0 \alpha + Y_1^1 \beta)$
	−1/2	$\frac{1}{\sqrt{3}}(Y_1^{-1} \alpha + \sqrt{2} Y_1^0 \beta)$
	−3/2	$Y_1^{-1} \beta$

Fig. 9. A sketch of the physical origin of L-edge XMCD in the two-step model.

These matrix elements are then evaluated for specific d-orbitals in spherical symmetry ($Y_2^{m_l}\beta$), and the oscillator strength for different edge and polarization combinations is calculated by summing over $m_l = -2, -1, 0, 1,$ and 2:

$$I_{L_3}^+ = \sum_{i,f} |\langle f | P_1^{(1)} | i \rangle|^2 = \frac{1}{3} R^2, \quad I_{L_3}^- = \frac{5}{9} R^2,$$
$$I_{L_2}^+ = \frac{1}{3} R^2, \quad \text{and} \quad I_{L_2}^- = \frac{1}{9} R^2 \tag{7}$$

Finally, the XMCD effect, for transitions solely to spin-down orbitals, is given by $\Delta I = I^+ - I^-$. For the L$_3$-edge, $\Delta I_{L_3} = -(2/9)R^2$, while at the L$_2$-edge, $\Delta I_{L_2} = +(2/9)R^2$. The key result from these calculations is that with lcp (using our 'optical' definition), at the L$_3$-edge the atom preferentially (5/8 of the time) emits spin-up electrons, while at the L$_2$-edge the atom preferentially (3/4 of the time) emits spin-down electrons (Fig. 9). This can be measured directly with spin-polarized circular dichroic photoemission [66,67].

The one-electron model can also be used to explain the spin polarization of K-edges. In these cases, spin-orbit coupling of the final state p-electron is invoked [22,68]. However, as noted by Brouder and Hikam [69], at K-edges the relative amounts of spin-up and spin down states depend on the absorbing atom, the neighboring atoms, and the energy above threshold. Because spin-orbit coupling is much weaker, the degree of spin-polarization is typically 1% or less.

3.1.1. Band theory and XANES XMCD

Once the spin polarization of the 'emitted' electron is established, the one-electron model can be used to explain XMCD effects in both the XANES and EXAFS regions. In the two-step model, the p$_{1/2}$ and p$_{3/2}$ shells are viewed as spin-polarized sources, and vacant spin-up and spin-down 3d bands are viewed as spin-sensitive 'detectors'. For example,

(assuming no orbital angular momentum) if only spin down states are available, then the 'asymmetry', $(\sigma^+ - \sigma^-)/(\sigma^+ + \sigma^-)$, at the L_2-edge should be a 50% effect, twice as large as at the L_3-edge (and opposite in sign). The simplest case, the rigid band 'Stoner model', is illustrated in Fig. 9.

In a more sophisticated analysis, multiple scattering calculations using FEFF8 source code reproduced most of the Ni metal $L_{2,3}$ XMCD, including a controversial satellite 6 eV above the main resonance [70]. The latter peak was missing using a 13-atom cluster, but appeared in the 50-atom calculation. A lower energy feature at 3 eV was assigned to many body effects. The authors point out that no approach yet captures all the physics in the XMCD effect. We note that an alternative approach using the configuration interaction model can also reproduce both the 6 eV XAS satellite and the 3 eV XMCD feature [71,72].

3.1.2. Scattering theory and EXAFS XMCD

The EXAFS region is also sensitive to the spin polarization of emitted electrons—scattering by magnetic neighbors depends on the photoelectron polarization. When the neighboring atom is spin polarized, there will be an exchange contribution in addition to the Coulomb scattering potential. This will modify both the amplitude $f_0(\pi, k)$ and phase shift $\phi_0(k)$ for electron backscattering, so that the traditional formula for EXAFS for a single absorber-scatterer interaction requires modification. Schütz and coworkers proposed addition of corrective terms $f_c(\pi, k)$ and $\phi_c(k)$ for the magnetic backscattering amplitude and phase shift, scaled by the degree of photoelectron polarization σ_z [68]:

$$\chi(k) = \frac{e^{-2\sigma^2 k^2} \, e^{-R/\lambda}}{kR^2} \, |f(\pi, k)| \, \sin[2kR + \phi(k)] \qquad (8)$$

where

$$f(\pi, k) = f_0(\pi, k) \pm \langle \sigma_z \rangle f_c(\pi, k) \quad \text{and}$$
$$\phi(k) = \phi_0(k) \pm \sigma_z \phi_c(k) \qquad (9)$$

The other terms have their conventional meaning: R is the absorber-scatterer distance, σ is the rms variation in R, k is the photoelectron wave number, and λ is its mean free path.

3.2. Ligand field multiplet theory (LFMT)

Ligand field multiplet theory is a multi-electron viewpoint that describes the initial and final states as multiplets that are mixed and split by the symmetry of the ligand field [73–77]. In this approach, the XMCD effect emerges naturally as a consequence of angular momentum selection rules. Spectra have been calculated for $3d^1$ through $3d^9$ systems with a range of crystal field and spin-orbit coupling strengths [78,79], so for many inorganic systems one can check beforehand to see if XMCD will be useful. Before discussing this in detail, it is worth illustrating the differences between one electron and multiplet approaches using the same
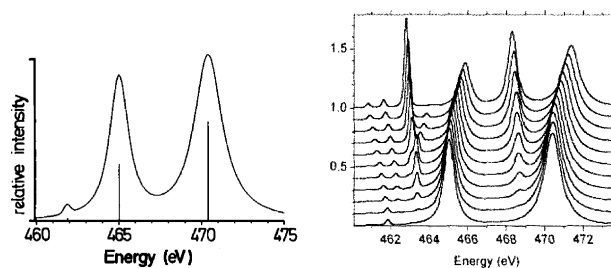

Fig. 10. The $2p^6 3d^0 \rightarrow 2p^5 3d^1$ transitions for a d^0 system (Ti^{4+}) in (left) spherical symmetry with p–d coupling and (right) with p–d coupling and variable octahedral ligand field (10Dq). 10Dq is 0 for lowest curve and increases in 0.3 eV steps to 3.0 eV for top curve. Reprinted with permission from [76]. Copyright (1990), American Physical Society.

$2p^6 3d^0 \rightarrow 2p^5 3d^1$ transition that was discussed with one-electron theory.

In the L–S coupling scheme, the closed shell ground state for a d^0 system such as Ti^{4+} has zero spin and orbital angular momentum, $S = L = 0$, hence this is a ^1S term and the only level is $^1S_0$. For the $2p^5 3d^1$ final state configuration, there are 12 possible levels—the triplets: $^3P_{0,1,2}$, $^3D_{1,2,3}$, $^3F_{2,3,4}$, and the singlets: $^1P_1$, $^1D_2$, $^1F_3$. In the absence of any final state coupling, the ΔJ selection rule ($\Delta J = 0, \pm 1$, no $0 \rightarrow 0$) allows only a single transition: $^1S_0 \rightarrow {}^1P_1$ (Fig. 10). Turning on the 2p spin-orbit interaction mixes the different L–S levels, and produces two accessible levels, a 'triplet' at $-(1/2)\xi_p$ and a 'singlet' at $+\xi_p$. The relative strengths are the familiar 2:1 ratio. So far, the results are the same as for the one-electron picture.

LFMT predictions diverge from the one-electron picture when interactions between partially filled $2p^5$ and $3d^N$ shells are included. These 'Coulomb' and 'exchange' interactions, described by the Slater–Condon parameters F^2, G^1, and G^3 [80], cause additional mixing of terms, so that the lowest energy (mostly triplet) level acquires some $^1P_1$ character. Thus, as nicely illustrated by DeGroot, even in spherical symmetry, LFMT predicts additional features that cannot be explained by one-electron theory (Fig. 10).

If one next turns on the ligand field portion of the theory, then J is no longer a 'good quantum number', and further mixing of levels occurs. In an O_h field, the symmetry of the initial state is A_1, the dipole operator is T_1, and final states must also have T_1 symmetry. It turns out there are seven such levels—four derived from the 10Dq splitting of the two main peaks, and an additional three transitions not explained in one-electron theory [76]. (The branching from $O_3 \rightarrow O_h$ is explained in Butler [81].) The seven predicted features are observed in d^0 systems such as KF, CaF_2, $FeTiO_3$ and ScF_3 [76], and their prediction and confirmation in such systems was one of the initial successes that helped confirm the utility of the LFMT approach.

Of course, for d^0 systems, there are no magnetic effects. What does LFMT have to say about the paramagnetic systems of interest in materials science and (bio)inorganic chemistry? For transition metal XMCD, the simplest case is

the $2p^63d^9 \to 2p^53d^{10}$ transition seen with Cu(II) and Ni(I) complexes, as explicated in a classic paper by van der Laan and Thole [79]. They begin by writing the initial and final states of an atom in a magnetic field as $|\alpha JM\rangle$ and $|\alpha' J' M'\rangle$, where J and M are the total angular momentum and magnetic moment respectively, and α designates all other quantum numbers. They note that the temperature-dependent line strength is given by:

$$\left\langle S^q_{\alpha J, \alpha' J'} \right\rangle = \left\langle A^q_{JJ'} \right\rangle \left| \left\langle \alpha J \left\| C^{(1)} \right\| \alpha' J' \right\rangle \right|^2 \qquad (10)$$

where the last factor is the line strength of the $\alpha J \to \alpha' J'$ transition, and the geometric factor $\left\langle A^q_{JJ'} \right\rangle$ distributes this intensity over the different $M \to M'$ transitions:

$$\left\langle A^q_{JJ'} \right\rangle = \frac{\left[\sum_M \begin{pmatrix} J & 1 & J' \\ M & q & M \end{pmatrix}^2 e^{-M/\theta} \right]}{\sum_M e^{-M/\theta}} \qquad (11)$$

In the last equation, θ is the reduced temperature, $\theta = kT/|g\mu_B|H$, and the squared term in the summation is a '3j symbol' [82]. Once the wave function is described in terms of M and J, the $T = 0$ XMCD intensities derive from the angular momentum algebra contained in the 3j symbol.

Life is simple in spherical symmetry. The initial d^9 ^2D term is split by spin-orbit coupling into $^2D_{3/2}$ and $^2D_{5/2}$ levels by the 3d spin-orbit interaction, and in a magnetic field; the latter is split by the Zeeman effect into six distinct states. At $T = 0$, there is only one allowed transition, $^2D_{5/2}$ ($M_J = -5/2$) $\to$ $^2D_{3/2}$ ($M_J = -3/2$), thus $\Delta M_J = q = +1$. This corresponds with absorption of lcp X-rays with our optical definition (Fig. 11).

Of more interest to chemists is the effect of a ligand field on the energies and intensities of different transitions. For example, for Cu^{2+} in D_4 symmetry, the wave function can have B_1, A_1, B_2, and E irreducible representations [83]. Further splitting by spin-orbit coupling and a magnetic field along the z-axis yields a Γ_8 ground state that is a mixture of $|5/2, 3/2\rangle$, $|5/2, -5/2\rangle$, and $|3/2, 3/2\rangle$ levels [79]. When the spin-orbit splitting is small compared to crystal field splittings, first order perturbation theory gives the ground state wave function as [79]:

$$|\Gamma_8\rangle = |B_1\rangle + \zeta_d/\Delta(B_2) |B_2\rangle + (1/\sqrt{2})\zeta_d/\Delta(E) |E\rangle \quad (12)$$

To give the reader the flavor of the information content of these spectra, the results of the van der Laan and Thole analysis are reproduced in Table 3. Note the major difference between LFMT and 'two-step' predictions. In the absence of ground state spin orbit coupling, LFMT predicts a branching ratio of 1 for $q = -1$ (a 100% XMCD effect at the L_2-edge). In contrast, we have seen that one-electron theory predicts at most a 50% asymmetry.

The complexity of XMCD spectra increases rapidly as: (a) the number of d-electrons nears a half-filled shell, (b)

Table 3
Line strength and branching ratio for d^9 system with Γ_8 character in C_4 symmetry

Dipole excitation	Line strength (P)	Branching ratio (B)
Isotropic	1/5	$[2 + 2\zeta_d/\Delta(b_2) + \zeta_d/\Delta(e)]/3$
$q = +1$	$[1 - 2\zeta_d/\Delta(b_2)]/10$	$[1 - 2\zeta_d/\Delta(b_2) + 2\zeta_d/\Delta(e)]/3$
$q = -1$	$[1 + 2\zeta_d/\Delta(b_2)]/10$	1
$q = 0$	$[\zeta_d/\Delta(e)]^2/20$	1

charge-transfer effects require inclusion of multiple configurations, (c) lower symmetry requires inclusion of orientation dependence, and (d) zero field splittings (which arise from 3d spin-orbit coupling effects) complicate the magnetic field dependence. Since this is a primer and not an encyclopedia, we merely mention potential complications and point the interested reader toward the relevant literature.

First of all, the calculations become more complex towards the middle of the transition series. As noted by deGroot, there are 1512 possible final states for a $2p^53d^5$ final state (for example, a Mn^{3+} initial state) [84]! Furthermore, in lower symmetry structures, additional parameters (Ds, Dt) are required to describe the ligand field, and the potential for artificially good simulations rises proportionally.

Van der Laan [85] has pointed out that in C_1 symmetry, the XMCD is a sum over three fundamental spectra, and that measurements in four different geometries are required. van Elp and Searle [86] have discussed how the XMCD can vary dramatically for different molecular orientations with respect to the magnetic field, especially when there is a zero field splitting comparable or larger than the applied Zeeman splitting. Finally, if charge transfer is significant between the metal ion and the ligands, then two or more configurations (e.g. $3d^N$, $3d^{N+1}L$) may be required to describe the electronic structure of both the initial and final states. Configuration interaction will add additional free parameters to the spectroscopic model. Given the potential complications to spectral simulation, it is fortunate that an alternate approach exists that requires far fewer assumptions—sum rule analysis.

3.3. Sum rule analysis

Sum rules are equations based on integrated spectra, and they allow derivation of valuable information without resort to laborious simulation techniques [87,88]. For example, most chemists are familiar with the Kuhn–Thomas sum rule, which states that the sum of oscillator strengths f_{no} is equal to the number of electrons N_e [89]:

$$\sum_n f_{no} = N_e \qquad (13)$$

The first X-ray sum rule to consider states that the integrated intensity over particular absorption edges reflects the number of empty states with the appropriate symmetry for the transition [90]:

$$\int_{j_++j_-} (\mu_0 + \mu_1 + \mu_{-1}) \, d\omega \propto \frac{4l+2-n}{2l+1} P^2_{c1l} \qquad (14)$$
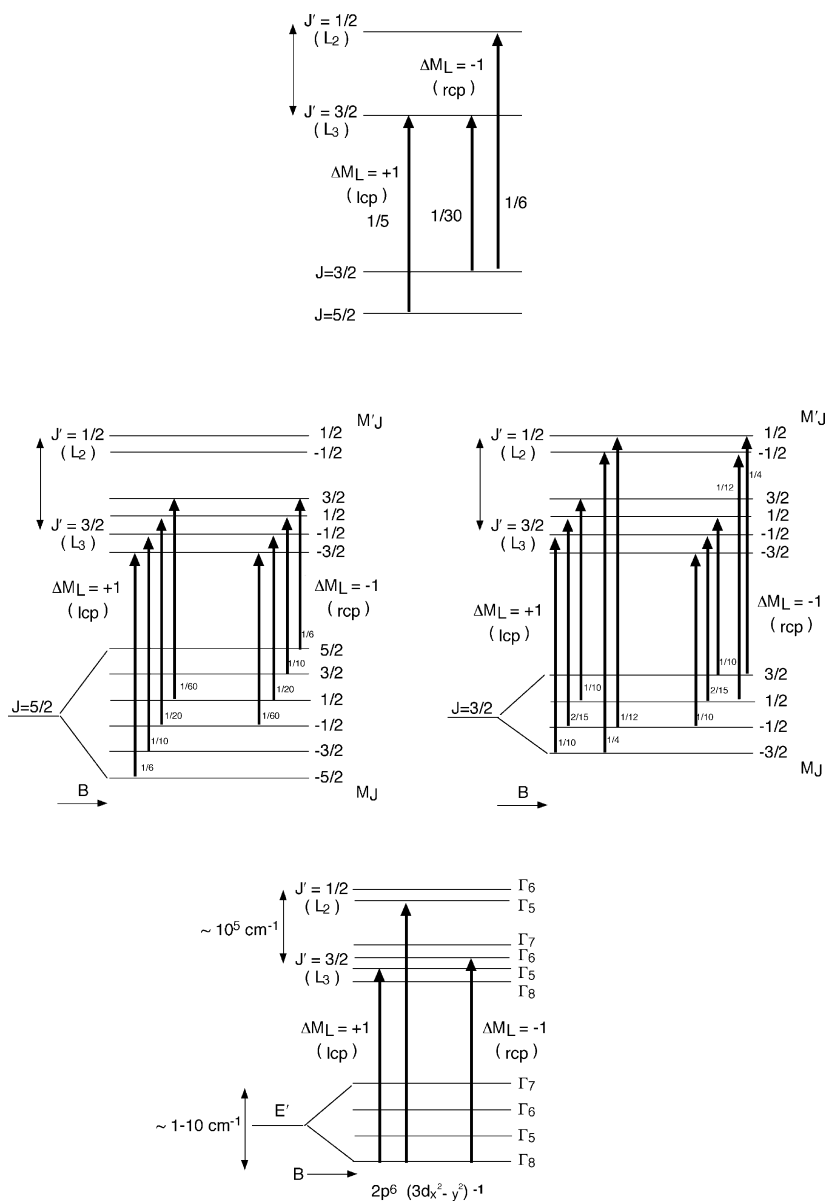
Fig. 11. XMCD transitions for atomic and molecular Cu(II). Fractions next to arrows are relative intensities. (Top) Dipole transitions in spherical symmetry, after van der Laan and Thole [79]. (Middle) Left- and right-circularly polarized transitions for d^9 configuration in magnetic field. (Bottom) Ground state circularly polarized transitions for d^9 in C_4 symmetry (D_{4h} plus magnetic field). In each case, the lcp transitions are grouped on the left and the rcp transitions on the right.

For transition metal $L_{2,3}$-edges, which have an initial 2p level, the transitions are primarily to states of 3d-symmetry, since the 2p $\rightarrow$ 4s transitions are ~20-fold weaker than the 2p $\rightarrow$ 3d transitions [1]. The decrease in the number of d-vacancies across the first transition series is nicely illustrated by comparing the white line intensities of the pure metals (Fig. 12) [56]. We have used this sum rule to quantify the amount of electron density transferred from copper to its ligands in blue copper proteins [91] and the Cu_A site, as well as the number of 3d vacancies in compounds with different Ni oxidation states [92].

For XMCD, the most important sum rules involve projections of the spin $\langle S_z \rangle$ and orbital $\langle L_z \rangle$ angular momentum of the absorbing species. In general terms:

$$\delta = \frac{\int_{j_+} (\mu_1 - \mu_{-1})\, d\omega - \frac{c+1}{c}\int_{j_-}(\mu_1 - \mu_{-1})\, d\omega}{\int_{j_+ + j_-}(\mu_0 + \mu_1 + \mu_{-1})\, d\omega}$$

$$= \frac{l(l+1) - 2 - c(c+1)}{3c(4l+2-n)}\langle S_z \rangle \hbar + \alpha \langle T_z \rangle \hbar \qquad (15)$$

and

$$\rho = \frac{\int_{j_+ + j_-}(\mu_1 - \mu_{-1})\, d\omega}{\int_{j_+ + j_-}(\mu_0 + \mu_1 + \mu_{-1})\, d\omega}$$

$$= \frac{1}{2}\frac{l(l+1) + 2 - c(c+1)}{l(l+1)(4l+2-n)}\langle L_z \rangle \hbar \qquad (16)$$
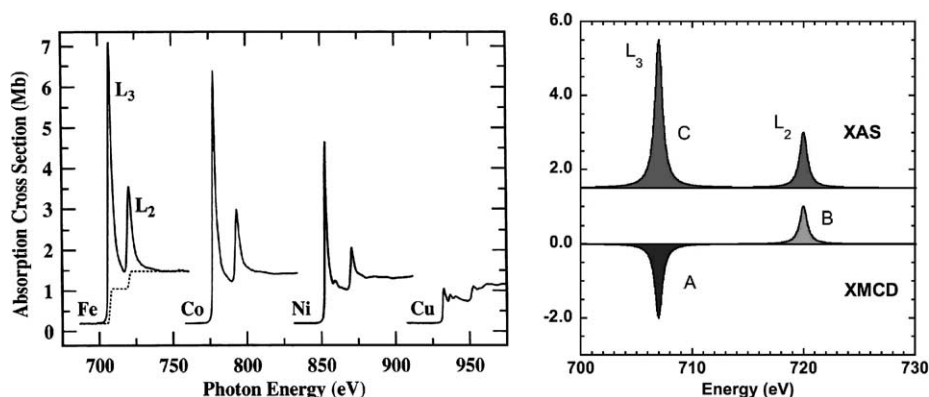
Fig. 12. (Left) White-line intensities of some first transition metals. (Right) Important quantities in hypothetical L-edge XMCD (right) spectra. A and B are the integrated areas under the XMCD L_3 and L_2-edge features, while C is the integrated area under the XAS absorption curves.

Stöhr and König have shown that $\langle T_Z \rangle$ angular averages to zero in 'powder' samples [93], so the last term in Eq. (15) can often be omitted. The quantities involved in sum rule analysis are illustrated graphically in Fig. 12.

Using these A, B, and C to represent the appropriate integrals (Fig. 12), neglecting the $\langle T_z \rangle$ term, and assuming that $\mu_0 = (\mu_1 + \mu_{-1})/2$ [94], yields the following simple expressions for the sum rules.

$$\langle L_z \rangle = \frac{2(A+B)}{3C} n_h, \qquad \langle S_z \rangle = \frac{A - 2B}{2C} n_h \qquad (17)$$

The sum rules have been tested by comparison with experimental measurements [53,56] and theoretical calculations [95,96]; they are generally thought to be accurate within about 10%. One possible source of error is found for the early transition metals, such as Cr, where the multiplet effects are larger than the 2p spin-orbit coupling and hence the L_2 and L_3-edges cannot be separated. Sainctavit et al. [97] have done analytical calculations for Cu(II) in an octahedral ligand field that address the sum rule assumptions. They found that at low temperature, the $\langle T_Z \rangle$ term makes a large contribution to the spin sum rule and cannot be ignored. Others have shown that $\langle T_Z \rangle$ can also be significant for other first transition metals, especially at lower symmetry surface sites [98].

4. Chemical and materials science applications of XMCD

There is now a very large literature of XMCD applications, the majority of which involve the characterization of magnetic materials. In a brief review, it is impossible to cover all of this literature, so below we simply illustrate some of the bioinorganic applications and highlight how XMCD is being used in materials science. Note that all of the (bio)inorganic XMCD examples arise from paramagnetic properties, and measurement of these spectra require liquid helium temperatures and magnetic fields of several Tesla. In contrast, many of the materials science examples involve ferromagnetic samples that are magnetized by much smaller fields and which can be measured at much higher temperatures. In both cases, however, the key spectroscopic advantages of XMCD are much the same.

4.1. Element specific detection of magnetic moments

A simple example of a bioinorganic application of XMCD involves the Ni derivative of the 'blue' Cu protein *Pseudomonas aeruginosa* azurin (NiAz) [99,100], a system we have studied in collaboration with Gray and co-workers [101]. Ni azurin can potentially serve as a model for more complex Ni sites such as those observed in H_2ase [NiFe], CODH C, and ACS A-clusters [102,103]. The Ni L-edge XMCD clearly shows the Ni(II) center is paramagnetic (Fig. 13); the spectra and simulations indicate that the Ni has a high-spin, triplet, ground state. The XAS and XMCD spectra have been calculated using the 3d orbital splitting pattern obtained from density functional theory (DFT) calculations as the basis for ligand field multiplet simulations (Fig. 13). Similar L-edge and XMCD studies have also provided evidence for high spin Ni(II) in NiFe H_2ases [104] and in certain forms of the C-clusters [105] and A-clusters [106].

Ni L-edge XMCD is playing a useful role in investigating the magnetic properties of transition metal rare-earth alloys and compounds. For example, it has been used to site-selectively monitor the Ni magnetic moment in RNi_2, where R is a rare-earth element. Normally, the Ni moment disappears as the rare-earth (R) content increases up to the Laves phase. Recently, XMCD has shown that the Ni site in $GdNi_2$ retains an intrinsic magnetic moment even in Laves phase concentrations. Its antiparallel alignment with the Gd moment can also be observed from the $M_{4,5}$-edge XMCD (Fig. 14) [107]. This is discussed in the magnetic coupling section below.

XMCD also occurs at transition metal K-edges, although the dichroism is significantly weaker than at L and M-edges. For example, in rare-earth transition metal alloys of Ho_6Fe_{23} and Y_6Fe_{23}, the structure and intensity
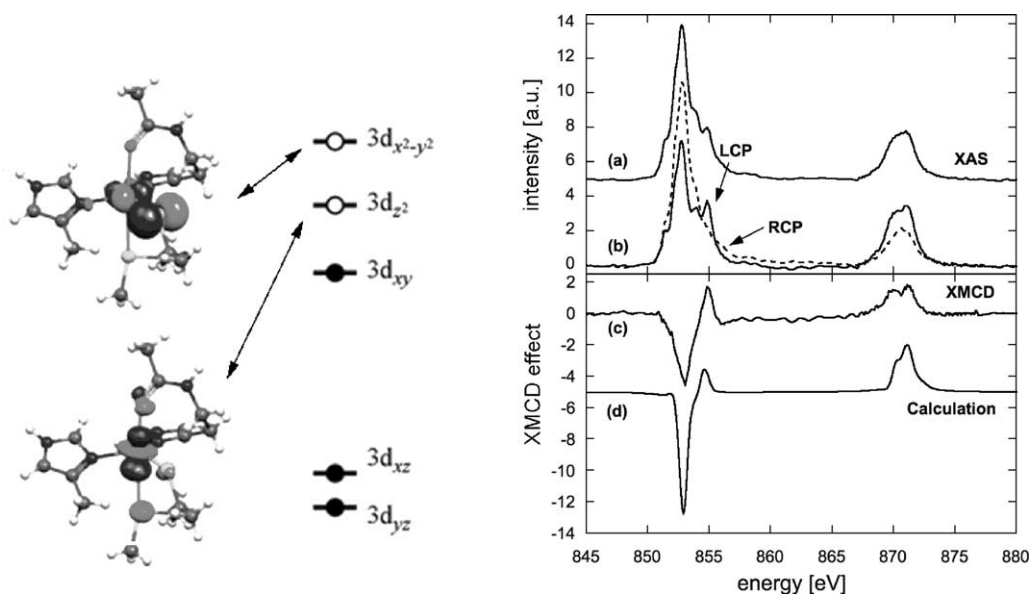
Fig. 13. (Left) Model of NiAz and orbitals involved in L-edge XMCD. (Right) XMCD data for NiAz at 6 T and 2 K. (a) Zero-field XAS spectrum. (b) rcp (- - - -) and lcp (—) XAS spectra. (c) XMCD spectrum. (d) Calculated XMCD. The L_3 centroid energy is 853.1(1) eV; the branching ratio is 0.722(4); and the magnetic moment is calculated to be 1.9(4)μ_B.

of Fe K-edge XMCD signals have been directly related to the Fe(4p,3d)-Ho(5d)/Y(5d) hybridized bands [108]. The shape of the Fe K-edge XMCD spectra of Y_6Fe_{23} (Fig. 14) closely resembles that of Fe metal (not shown). In contrast, the Fe K-edge XMCD for the Ho alloy shows significant differences, with an additional positive feature observed at about 7.118 keV. This has been attributed as an effect due to Ho, implying stronger Fe–Ho hybridization than in the Fe–Y case.

Another example of Fe K-edge XMCD involves H_2 absorption by intermetallic $R_2Fe_{14}B$ materials. These ex-periments are driven by interest in permanent magnet technology [109] and aim to distinguish the effects of hy-drogen on the iron sublattice magnetism from the effects on the rare-earth element. Fe K-edge XMCD spectra on $Nd_2Fe_{14}BH_x$ and $Y_2Fe_{14}BH_x$, show that increasing inter-stitial hydrogen content in the Y–Fe intermetallic has little effect on the Fe magnetic moment (Fig. 15). In contrast, the difference XMCD signal increases with hydrogen content for the Nd-Fe material, showing that the Nd contribution to the Fe magnetism decreases with the increase in hydrogen content.
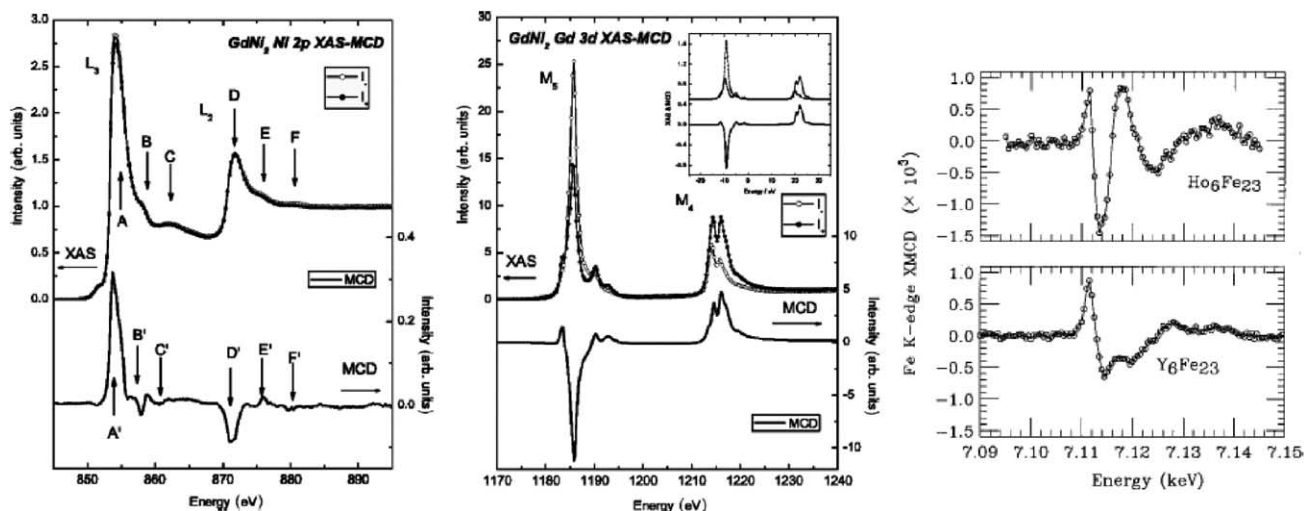

Fig. 14. (Left) Ni 2p → 3d XAS and XMCD spectra of $GdNi_2$, at a temperature of 25 K. (Center) Corresponding Gd 3d → 4f XAS-MCD spectra. The inset shows the theoretical XAS and XMCD spectra [107]. Reprinted with permission from [107]. Copyright (2003), by the American Physical Society. (Right) Fe K-edge XMCD spectra of Ho_6Fe_{23} and Y_6Fe_{23} alloys at room temperature. Reprinted with permission from [108]. Copyright (2000), American Institute of Physics.
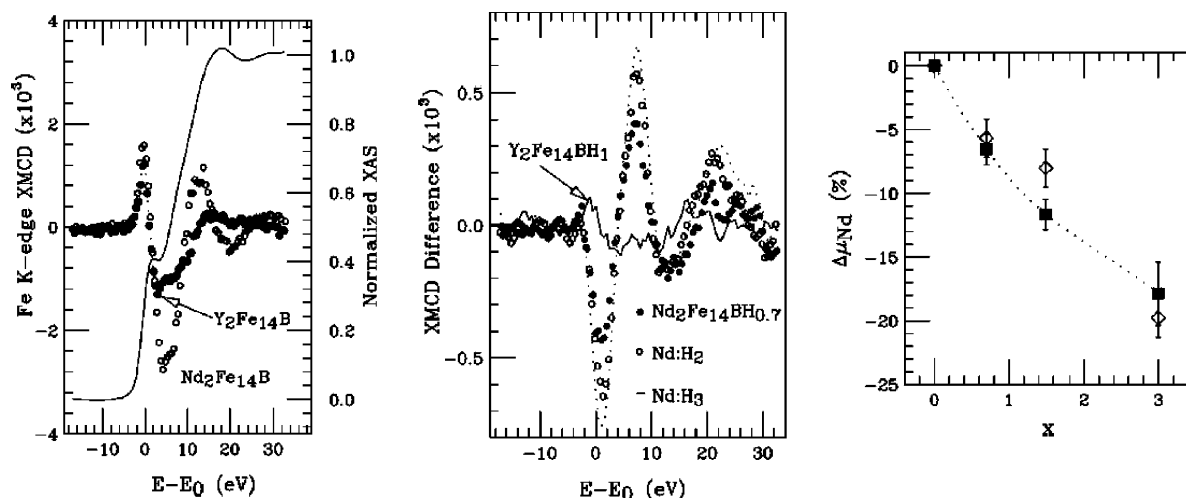
Fig. 15. (Left) Normalized XMCD spectra at the Fe K-edge, comparing $Y_2Fe_{14}B$ (●) and $Nd_2Fe_{14}B$ (○). The solid line is the normalized Fe K-edge XAS spectra for $Y_2Fe_{14}B$. (Middle) Fe K-edge Difference XMCD spectra of $Y_2Fe_{14}BH_1$ (solid lines) and $Nd_2Fe_{14}BH_x$, ($x = 0.7$ (●), $x = 2$ (○) and $x = 3$ (- - -)) obtained by subtracting the XMCD of the parent compound. (Right) Comparison of the Nd magnetic moment obtained from the magnetization measurements (■) and XMCD (◇) for the $Nd_2Fe_{14}BH_x$ hydrides with respect to the $Nd_2Fe_{14}B$. Reprinted with permission from [109]. Copyright (2003), American Institute of Physics.

A recent XAS/XMCD study of $CeRu_2Si_2$ [110] nicely illustrates magnetic effects at rare-earth L-edges. $CeRu_2Si_2$ is a typical 'heavy fermion' (HF) compound with an electronic specific-heat coefficient $\nu = 350\,mJ/K^2$ mol below $T_K = 20\,K$ [111]. This compound is reported to show a metamagnetic transition into a ferromagnetically ordered state induced by the magnetic field at 7.8 T below a temperature of 10 K [112]. Although such behavior among heavy-fermion systems is an important topic, this property in these systems is still not completely understood.

Honma and coworkers used Ce $L_{2,3}$-edge XMCD ($2p \rightarrow 5d$ transitions) to characterize unoccupied Ce 5d electronic states in $CeRu_2Si_2$ [110]. The Ce L_2-edge XAS (Fig. 16) of the trivalent $CuRu_2Si_2$ and $CuRu_2Ge_2$ systems exhibits a strong peak A arising from $2p \rightarrow 5d$ electric dipole transitions with $4f^1$ configuration and a weak shoulder B attribute to the $4f^0$ configuration [113]. A similar double peak structure A' and B' is observed in the tetravalent CeO_2 system. The XMCD (Fig. 16) shows a change around the white line qualitatively suggesting the decreasing c–f hybridization in $CeRu_2Si_2$ and that the 4f states are almost localized states of $Ce^{3+}(4f^1)$ similar to the $CeRe_2Ge_2$ system.

The Ce L_2 and L_3 XAS/MCD of $CeRu_2Si_2$ measured at magnetic fields lower and higher than the metamagnetic crossover field H_c (Fig. 16), showed an enhancement of the 'white line' of the Ce L_2-edge above the phase transition, suggesting weaker c–f hybridization and stronger localization of the 4f states in the ferromagnetic phase. Notice that even though the XMCD effect at these hard X-ray edges was less than 1%, an excellent signal-to-noise ratio was possible.

4.2. Deciphering mixtures

XMCD provides an extra tool for separating magnetic and non-magnetic components in an X-ray spectrum, as well as for distinguishing components with different magnetic moments. Real world samples are often inhomogeneous. In some spectroscopies, such as EPR, this is not a major problem—non-magnetic components do not give a signal, and overlapping spectra can be separated by exploiting different power saturation curves or by other methods. Inhomogeneity is more of a problem for conventional X-ray spectroscopy, where chemical shifts are relatively small compared to natural line widths and here XMCD can make real contributions.

For example, in collaboration with David Grahame, we have studied the β^*-subunit 'A-cluster' Ni site of *M. thermophila* ACDS protein [114]. This cluster is closely related to the active site for acetyl-CoA synthesis in the α subunit of carbon monoxide dehydrogenase/acetyl-CoA synthase (CODH/ACS) from *C. thermoaceticum*, where the first crystal structure revealed a unique $Ni–Cu–Fe_4S_4$ cluster (Fig. 17) [115]. A later structure found both $Ni–Zn–Fe_4S_4$ and $Ni–Ni–Fe_4S_4$ clusters in the same crystal [116], and it is now generally accepted that the Ni–Ni species is the active catalytic form [117].

Both high spin (paramagnetic) and low-spin (diamagnetic) Ni(II) have been proposed as constituents of various Ni enzymes [105,118]. When we examined the Ni L-edge spectrum of one particular sample, we observed a complex spectrum with at least three bands (Fig. 17) [106]. The XMCD spectrum showed that the low and high energy features were magnetic, and most likely represented two components of a single high-spin Ni(II) spectrum. The central peak did not show an XMCD effect and most likely represented low-spin Ni(II). Since Ni presumably occupies both 'external' sites in this particular protein, our working hypothesis is that the low-spin Ni occupies the more square planar 'M_b' site, while the high-spin Ni occupies the more tetrahedral 'M_a site' [106]. The observed heterogeneity
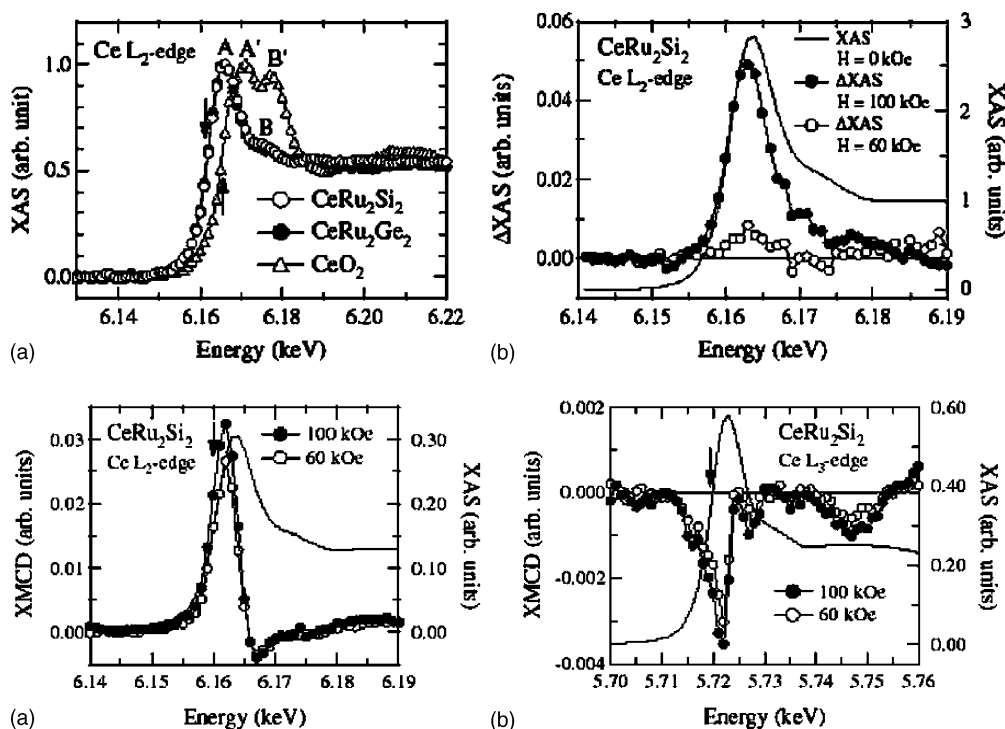
Fig. 16. (Upper panel) (a) Ce L_2-edge spectra for CeRu$_2$Si$_2$, trivalent CeRu$_2$Ge$_2$, and tetravalent CeO$_2$. Note the absorption-edge energy shift from CeRu$_2$Ge$_2$ to CeO$_2$ arises from the difference in Ce oxidation states. (b) The observed Ce L_2-edge XAS spectra at different fields of 6 T (60 kOe), 10 T (100 kOe), and zero field for CeRu$_2$Si$_2$. (Lower panel) XAS at zero field and MCD spectra at: (a) Ce L_2-edge and (b) Ce L_3-edge. Reprinted with permission from [110]. Copyright (2003), Institute of Physics.

would be hard to infer from the K-edge XANES or EXAFS alone.

4.3. Magnetic coupling

Since the sign of the XMCD effect reveals the net spin orientation for a given element or oxidation state, this technique can probe the interaction between different species in magnetically coupled systems. The easiest cases to study

are interactions between different elements, because the edges are usually well separated in energy. The first such application was a temperature dependent XMCD study of Fe$_3$Gd$_3$O$_{12}$ [119]. At room temperature, the primary Fe XMCD signal was negative, while the Gd signal was positive. This indicated that the bulk magnetic moment was dominated by the contribution from the Fe spins, and that the Gd was antiferromagnetically coupled to the Fe. At low temperature, the Gd M_3-edge showed a strong
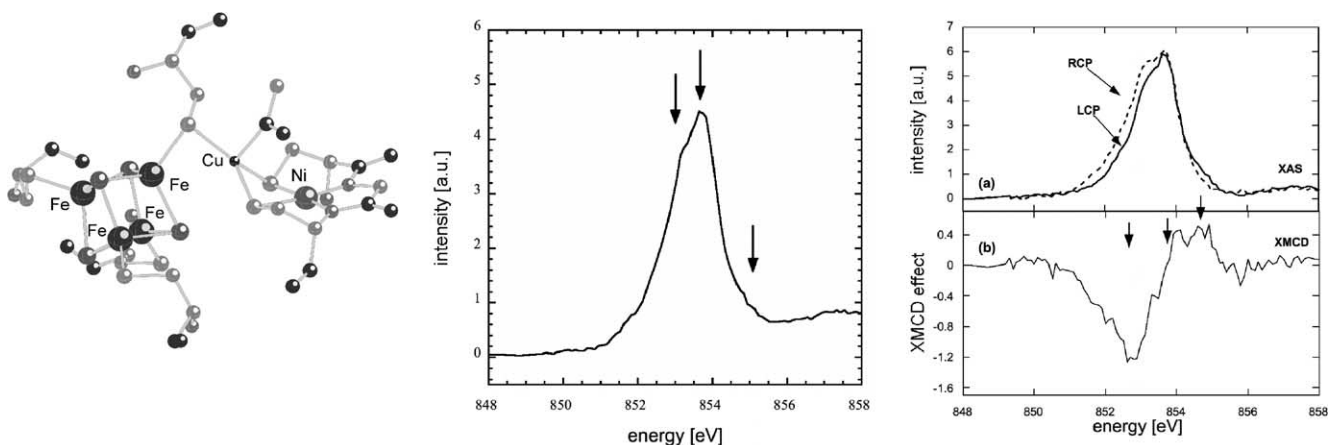

Fig. 17. (Left) The structure of the Ni–Cu form of the A-cluster [115]. The β*-subunit presumably has Ni in both proximal and distal sites. (Middle) Ni L absorption spectrum for the β*-subunit 'A-cluster' of *M. thermophila* ACDS protein. (Right) 6 T, 2 K XMCD spectrum for the same sample. Arrows indicate the bands discussed in text.
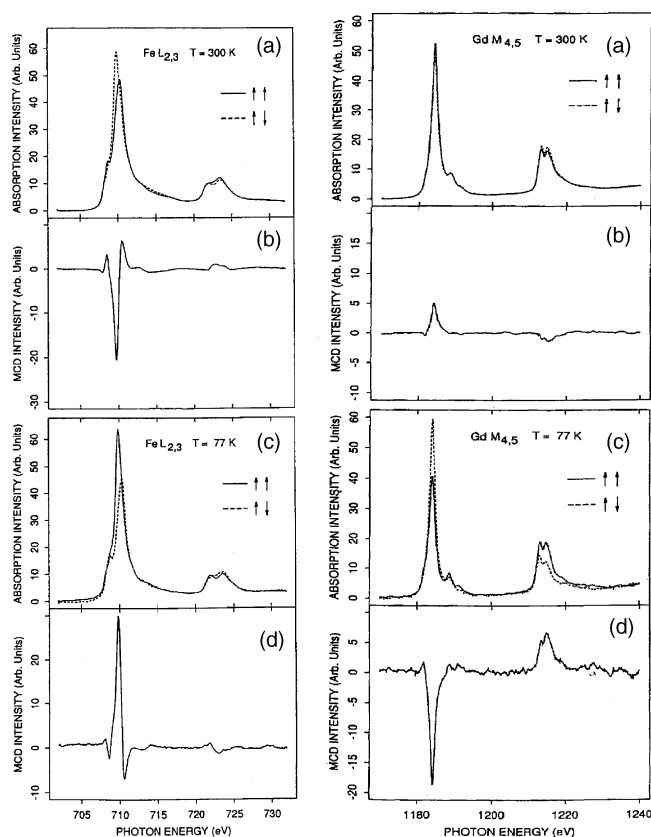
Fig. 18. The Fe L-edge (left) and Gd M-edge (right) XMCD spectra of $Fe_3Gd_3O_{12}$. Reprinted with permission from [119]. Copyright (1992), Elsevier Science.

negative XMCD, indicating that the Gd moment became the dominant factor, while positive Fe L_3-edge XMCD again indicated antiferromagnetic coupling (Fig. 18).

In collaboration with the Solomon and Karlin groups, we have used XMCD to observe antiferromagnetic coupling between Fe and Cu in Karlin's $[(F_8\text{-TPP})Fe^{III}\text{-}(O^{2-})\text{-}Cu^{II}\text{-}(TMPA)]^+$ complex (Fig. 19). This is an $S = 2$ system with antiferromagnetic coupling between $S = 5/2$ high-spin Fe(III) and $S = 1/2$ Cu(II). As expected, the Fe and Cu XMCD are of opposite sign.

XMCD analysis can also be used to study the magnetic coupling in mixed valence of the same element, provided there is a useful chemical shift between different oxidation states. Our long-term goal is to use XMCD for interpreting the spectra of complex clusters, such as the M center in nitrogenase [120] and the oxygen-evolving complex (OEC) of photosystem II [121]. As a model for the latter problem, we studied the C_{15}-carboxylate derivative of a 'single-molecule magnet' $Mn_{12}O_{12}(O_2CR)_{16}(H_2O)_4$ cluster system from George Christou's lab (Fig. 21) [122]. The spectrum shows a strong bipolar signal at both L_3 and L_2-edges. The negative XMCD at the L_3-edge is assigned primarily to the set of eight Mn(III) ions that are ferromagnetically coupled, while the positive signal at higher energy corresponds mostly to the central cube of four Mn(IV) whose magnetic

moments are predominantly opposite to the net magnetization.

Recently, Moroni and coworkers have studied a very similar system, $Mn_{12}O_{12}(O_2CR)_{16}(H_2O)_4$ with R–CH$_3$, which they abbreviate as Mn12-ac [123]. This paper illustrates both the valuable information content in XMCD of mixed-valence complexes as well as the complex analysis required for quantitative interpretation of these spectra. (A paper primarily concerned with sum rule analysis of Mn12 has also appeared [124].) The authors recorded XMCD at 1.5 K in a 4 T field using photocurrent yield detection and an asymmetric wiggler as a ∼60% polarized source. To assist in the interpretation, they also recorded XMCD of representative mononuclear Mn(III) and Mn(IV) complexes. These spectra were simulated using ligand field multiplet calculations with a single configuration and reduced Slater integrals.

XMCD powder spectra reflect an average of absorption cross sections over particular molecular orientations with respect to the magnetic field, and in principle a simulation should include these effects (much as is done in EPR simulations). However, the authors employ an approximate integration procedure developed by Ayant et al. [125], in which a powder spectrum is simulated by a sum over special orientations. The Mn(III) spectra were calculated in D_{4h} symmetry to account for the large Jahn–Teller distortion, while the Mn(IV) spectra were simulated under O_h symmetry. This lead to the following particular summations:

$$\sigma_{l(r)}^{Mn(III)} = \frac{1}{15}(2\sigma_{l(r)}^{[0\,1\,0]||B} + \sigma_{l(r)}^{[0\,0\,1]||B} + 4\sigma_{l(r)}^{[1\,1\,0]||B}$$
$$+ 8\sigma_{l(r)}^{[1\,0\,1]||B}) \quad \text{and} \quad \sigma_{l(r)}^{Mn(IV)}$$
$$= \frac{1}{15}(3\sigma_{l(r)}^{[0\,0\,1]||B} + 12\sigma_{l(r)}^{[1\,0\,1]||B}) \qquad (18)$$

One of the most interesting results from the model calculations was the highly anisotropic magnetic properties for the Mn(III) complex, for which a 4 T B field parallel to the 'hard' xy plane was insufficient to force magnetization of the complex (Fig. 20). In contrast, the magnetic properties and XMCD of the Mn(IV) complex were nearly isotropic (Fig. 20).

Turning to the Mn$_{12}$ XMCD, the calculations were done by assuming that all of the Mn(III) C_4 axes were parallel to each other, and then calculating a powder average. The Mn(IV) contribution was treated by assuming a superexchange field antiparallel to the magnetic moment of the Mn(III) ions, yielding a factor of $-1/2$ compared to the mononuclear XMCD. The general success of this model can be seen in the reasonably good agreement between experimental and calculated XMCD (Fig. 20). On the other hand, this work also brings home the complexity of the inverse analysis—could one infer the presence of an $S = 10$ antiferromagnetically coupled Mn(III)$_8$Mn(IV)$_4$ cluster from the XMCD alone?

We have observed even more complex XMCD in the weakly coupled Fe(II)Fe(III) system $[Fe_2(III,II)(bpmp)(\mu\text{-}O_2CC_2H_5)_2][BPh_4]_2$ (Fig. 21) [126]. In a 6 T field, both
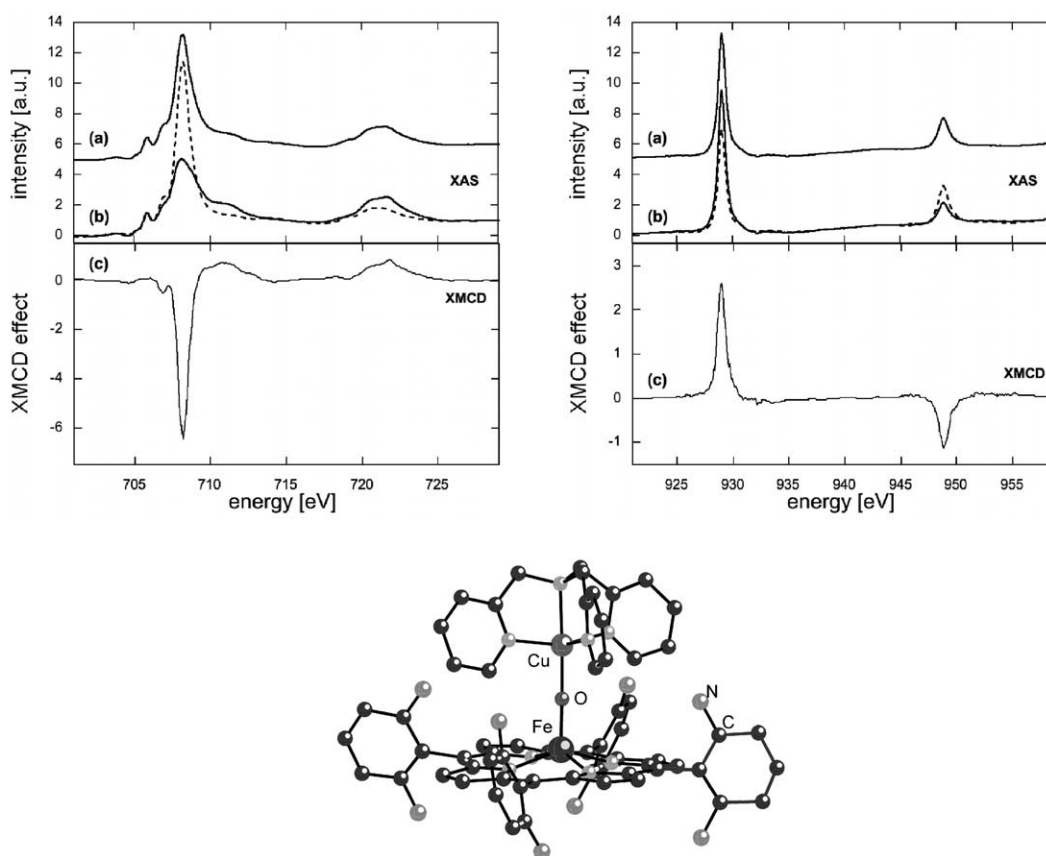
Fig. 19. XMCD for (Top left) Fe and (Top right) Cu L-edges measured at 2.2 K and 6 T for (bottom) Karlin's FeCu complex.

signals are negative, indicating that the spins are mostly parallel and that the Zeeman interaction overwhelms the zero field splittings D and the exchange interaction J_{AB}. The observed XMCD was ~34% of the effect expected for two independent and totally oriented Fe(II) and Fe(III) ions,

indicating that the temperature and field were not sufficient to achieve total spin alignment. In a weaker 1 T field, the Fe(II) XMCD became quite weak. There is a competition between the different terms in the spin Hamiltonian, but neglecting zero field splittings, the antiferromagnetically
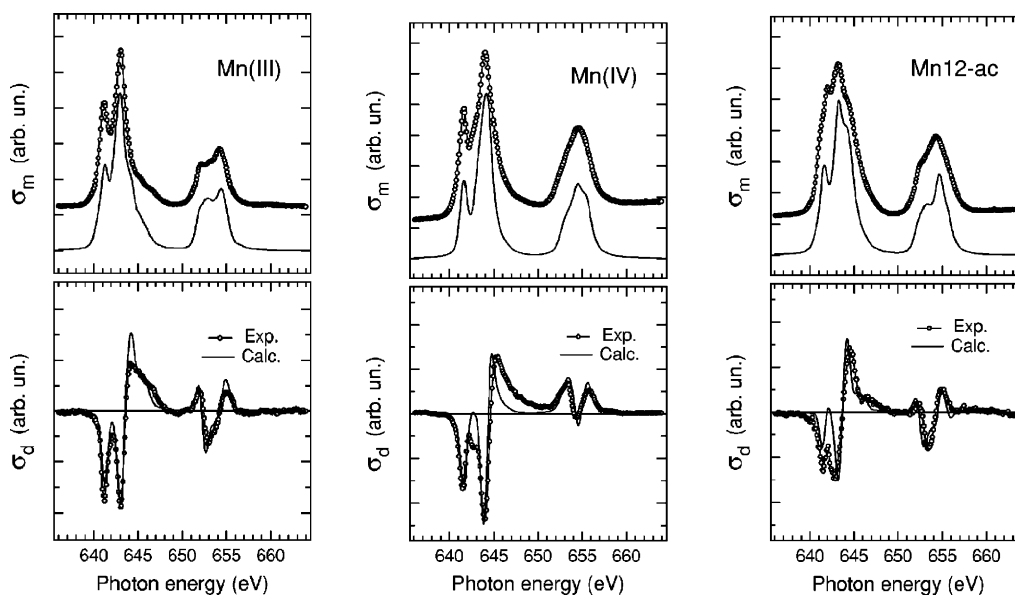

Fig. 20. (Left) Mn(III), (middle) Mn(IV), and (right) Mn-12 XMCD. Reprinted with permission from [123]. Copyright (2003), American Physical Society.
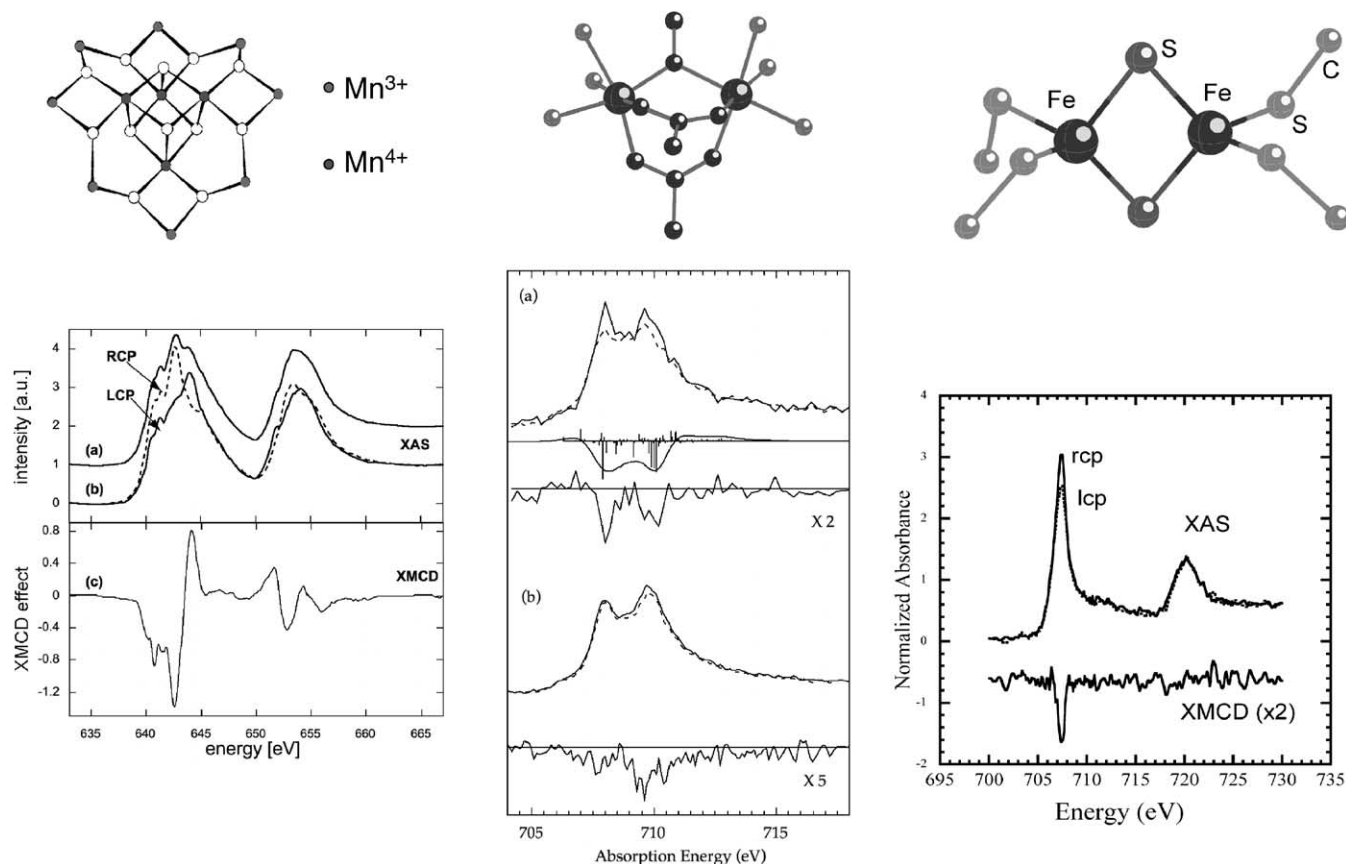
Fig. 21. XMCD of magnetically coupled systems of same element. (Left) XMCD for [Mn$_x$(III, IV] in 6 T field. Spectra with lcp (—) and rcp (- - -) and XMCD. (Middle) XMCD spectra for [Fe$_2$(III, II)(bpmp)(μ-O$_2$CC$_2$H$_5$)$_2$][BPh$_4$]$_2$ in different fields. (a) (Top) Spectra with left (- - -) and right (—) circular polarization; (middle) sum of calculated XMCD for Fe(II) and Fe(III); (bottom) experimental XMCD (b) XMCD at 1 T: spectra with lcp (- - -) and rcp (—) and XMCD spectrum [126]. Note that the relatively poor signal to noise is because this is one of the first paramagnetic XMCD spectra that used a low-flux beamline. (Right) The Fe(II)Fe(III) core of 2Fe ferredoxin and its XMCD in 6 T field and a temperature of 2.2 K.

coupled Fe(II) should eventually have a positive XMCD at a sufficiently weak magnetic field.

One of the most intractable systems we have encountered is the relatively 'simple' $S = 1/2$ Fe(II)Fe(III) site encountered in reduced 2Fe ferredoxins. Naïve subtraction of a reduced ($S = 2$) Fe(II) rubredoxin (Rd) XMCD from the oxidized $S = 5/2$ Fe(III) Rd spectrum yields a bipolar spectrum distinctly different from the experimental spectrum (Fig. 21). At least two factors complicate the naïve analysis. First, Mössbauer data show that the covalency of Fe in the binuclear site is such that chemical shifts between the ferrous and ferric site are significantly reduced from the 1.4 eV values observed in mononuclear Rd centers. Assuming a direct proportionality between isomer shift and L-edge shift, only ~0.5 eV is expected. Second, one must consider the spectra from all the possible M$_s$ states that give rise to the total $S = 1/2$. Not only is there a $M_{Fe(III)} = 5/2 + M_{Fe(II)} = -2$ contribution, but there are four other combinations (3/2, −1; 1/2,0; −1/2,1; −3/2,2) weighted in proportion to their Clebsch–Gordon coefficients [127].

A curious coupling example from materials science is in the non-oxidic colossal magnetoresistance (CMR) spinel Fe$_{0.5}$Cu$_{0.5}$Cr$_2$S$_4$, which exhibits very large negative magnetoresistance even at room temperature [128]. In this compound, L-edge XAS reveals that Fe is formally in the ferric state, Cr is trivalent and the Cu site is Cu(II). However, while XMCD reveals antiferromagnetic coupling between Fe and Cr as the XMCD signs are opposite, the XMCD at the Cu L-edge revealed that any magnetic moment at the Cu sites is very small if not zero ($<0.20\mu_B$) (Fig. 22).

4.4. Magnetic moments from sum rule analysis

Element specific magnetic spin moments have been one of the major applications of XMCD. Thanks to the 'charge', 'spin' and 'orbital sum rules' discussed above, simple integration of properly normalized spectra can reveal the number of vacancies and the magnetic moments. The first bioinorganic application of XMCD sum rule analysis involved the 'blue Cu' site in plastocyanin (Fig. 23). XMCD sum rule analysis has also been applied to Ni(II) sites in Ni-doped MgO (Fig. 23). For the plastocyanin work, application of the orbital sum rule yielded a Cu 3d specific $\langle L_Z \rangle$ of ~0.07$\hbar$ and $\langle S_Z \rangle$ of ~0.18$\hbar$ per Cu, both within 15% of values derived from SCF-Xα-SW calculations [129].

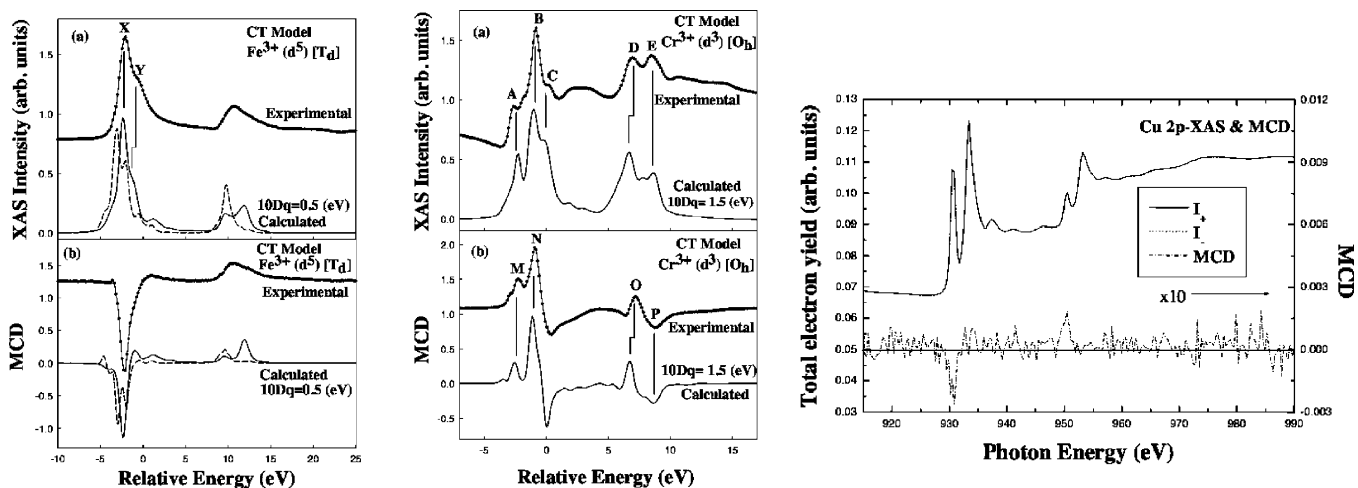Fig. 22. XAS and XMCD spectra of $Fe_{0.5}Cu_{0.5}Cr_2S_4$. (Left) Comparison of experimental (●) and calculated Fe L-edge: (a) XAS (b) XMCD. Calculations used charge transfer multiplet model at the Fe $L_{2,3}$-edges for the Fe^{3+} (full line) and Fe^{2+} (- - -) with 10Dq = 0.5 eV. (middle) Comparison of the experimental (●) and calculated Cr L-edge (a) XAS spectra (b) XMCD spectra. Calculations used 10Dq = 1.5 eV. (Right) XAS and XMCD (- - -) spectra at Cu L-edge for $Fe_{0.5}Cu_{0.5}Cr_2S_4$ [128].

4.5. Element-specific magnetization curves

The field and temperature dependence of the XMCD effect yield information about the magnetization of a sample that can be interpreted independently of one-electron or LFMT models. The advantage of X-rays over optical techniques such as the Kerr effect is that each element can be probed separately. An important technological application has been the study of the magnetization of different elements in magnetic multilayers, such as the 'spin-valve' heads used in modern high-density read heads [130]. These devices employ the giant magnetoresistance (GMR) effect to produce a large change in electrical current from a small change in applied field, thus allowing higher density information storage. We remind the reader that the magnetization of ferromagnetic samples can depend not only on temperature and the current applied field $\vec{H}$, but also on the previous values of $\vec{H}$; in other words, samples can exhibit 'hysteresis' [131].

For example, scientists at ESRF have studied a model trilayer system consisting of a (soft) 50 Å $Ni_{80}Fe_{20}$ layer, a variable thickness metallic Cu spacer, and a (hard) 50 Å Co layer, using fluorescence detected XMCD at the Ni and Co L_3-edges. With a thin (60 Å) Cu spacer and a slowly changing applied field, both Ni and Co reverse magnetization with the same coercive field, showing that the layers are strongly ferromagnetically coupled. With a thicker (100 Å)
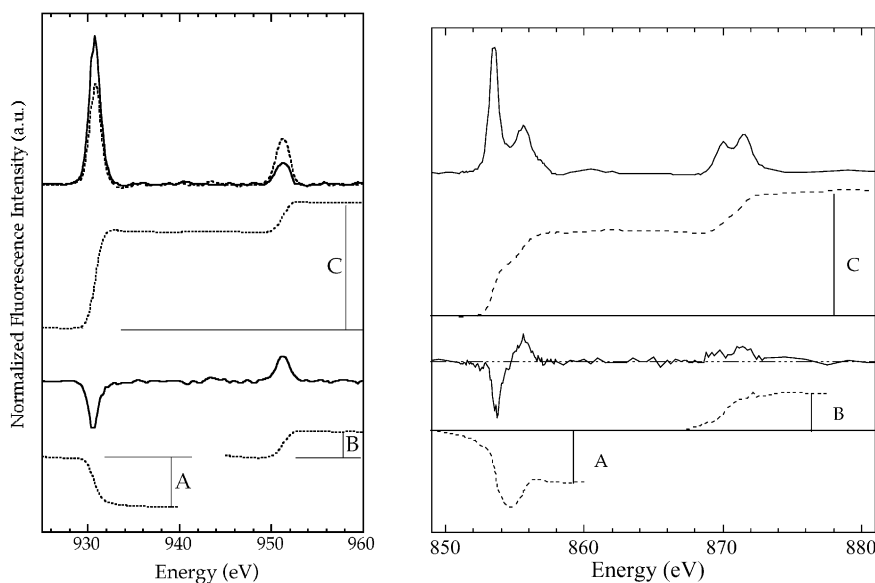

Fig. 23. (Left) XMCD spectra and sum rule integrations for the blue Cu site in plastocyanin. (Right) Absorption and XMCD spectra and sum rule integrations for the Ni(II) site in Ni-doped MgO.

Cu spacer, the $Ni_{80}Fe_{20}$ layer requires a much smaller coercive field—the magnetic layers have become decoupled. By employing a pump-probe technique, the authors were able to observe the dynamics of the magnetization process on a nanosecond time scale [132].

For the paramagnets of interest in (bio)inorganic chemistry, the simplest model for the magnetization of N interacting atoms in volume V is given by $M = M_0 B(x, J)$, where M_0 is the saturation magnetization, $x = (gJ\mu_B H)/(kT)$ and $B(x, J)$ is the Brillouin function:

$$B(x, J) = \frac{2J+1}{2J} \coth\left(\frac{2J+1}{2J}x\right) - \frac{1}{2J}\coth\left(\frac{1}{2J}x\right) \tag{19}$$

which reduces to XMCD $\sim \tanh[(gJ\mu_B H)/(kT)]$ for $S = 1/2$ systems with no orbital moment [131]. The curves in Fig. 19 and Fig. 24 illustrate the potential of XMCD magnetization curves as a characterization tool separate from sum rule analysis and multiplet simulations. Magnetization curves should be especially useful for the analysis of mixtures, where different uncoupled species might magnetize at different rates.

Of course, as noted by Pavel and Solomon [133], systems with zero field splittings such as Fe(II) can exhibit far more complex magnetization curves. Only recently has the quality of magnetization curves improved enough to warrant a more sophisticated analysis.

4.6. Element specific magnetic microscopy

All of the strengths of XMCD can in principle be combined with spatially resolving instruments to obtain element-specific images of magnetic properties [45,112,134]. These microscopes can generally be divided into three types: (a) scanning instruments, in which a focused X-ray spot is raster-scanned across the sample and the transmission or secondary yield of fluorescence or photoelectrons is recorded, (b) imaging transmission microscopes, that operate in a mode similar to transmission light microscopes, with the condenser and analyzer lenses replaced by zone plates for the X-ray region, and (c) photoelectron microscopes, in which the photoelectron yield from different regions of the sample is imaged through electron microscope optics (Fig. 25).
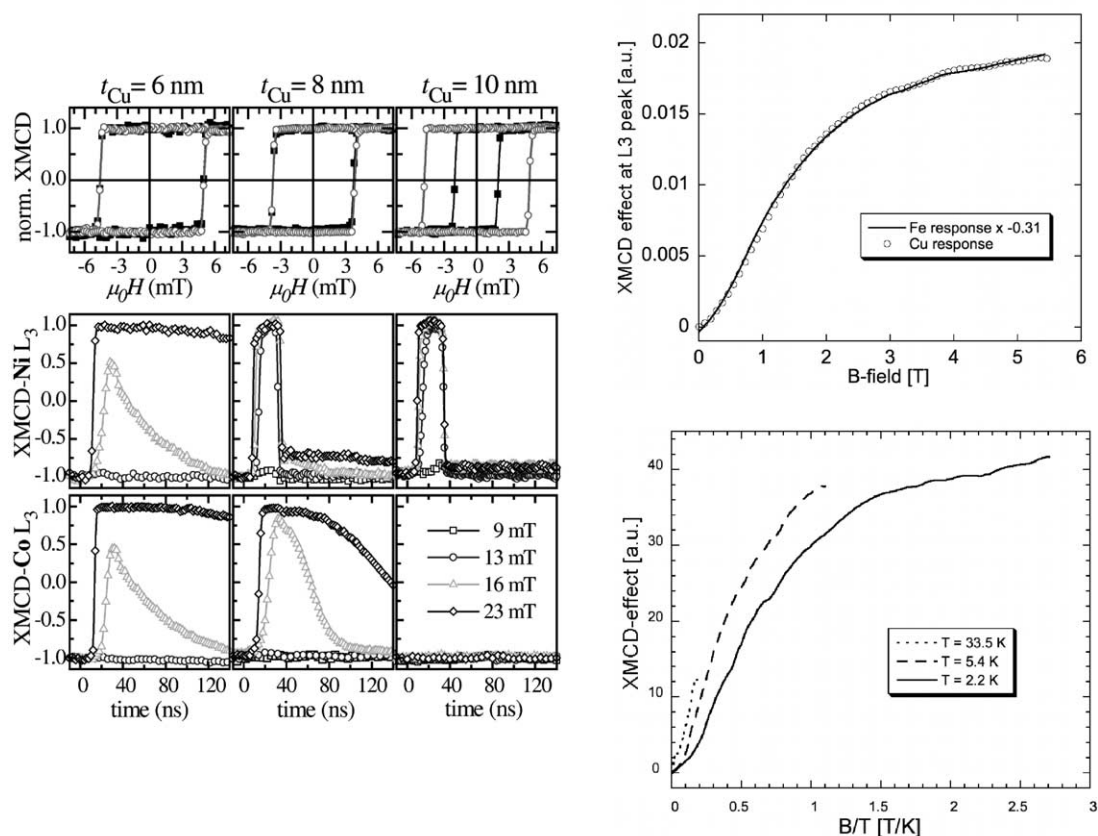

Fig. 24. (Left, top) XMCD magnetization curves obtained on the $Ni_{80}Fe_{20}$/Cu/Co trilayer system. Ni XMCD—filled circles, Co XMCD—open circles. (Left, bottom) Time dependence of Co and Ni magnetization. Reprinted with permission from [132]. Copyright (2001), American Physical Society. (Right) XMCD magnetization curves for the FeCu complex discussed in Fig. 19. (Upper-right) Normalized XMCD magnetization curves for the Fe(III) and Cu(II) L_3-edges. Clearly, the element specific magnetizations superimpose for this coupled system. (Lower-right) Temperature dependent magnetization curves for the Fe(III) L_3-edge.
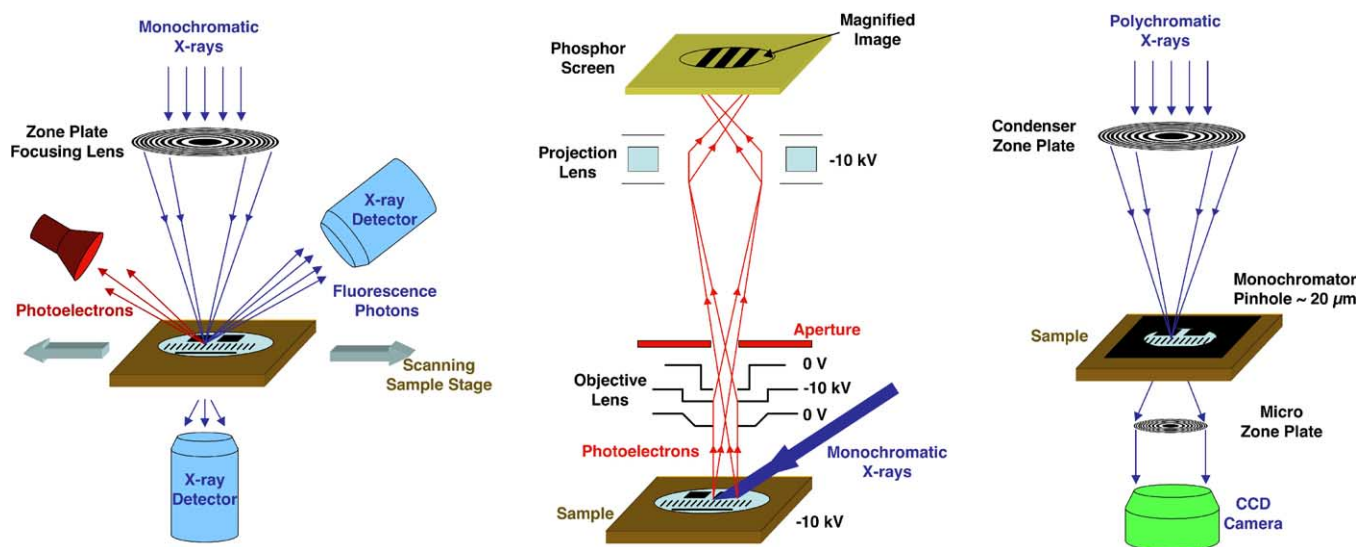
Fig. 25. Schematic illustration of (left) a scanning X-ray microscope, (middle) a photoelectron microscope and (right) an imaging transmission microscope.

XMCD–photoemission electron microscopy (XMCD–PEEM) is a powerful tool to examine element-specific magnetism. For example, in the search for new materials for use in 'spintronics' applications, 'half-metallic ferromagnets' (HFM) are among the desirable targets. These materials have one spin channel (up or down spin) that is metallic, while the other spin channel has a gap at the Fermi level. This causes complete polarization of the conducting electrons. Recent calculations predicted that the Heusler compound $Co_2Cr_{0.6}Fe_{0.4}Al$, an electron-doped derivative of Co_2CrAl, would exhibit a total spin polarization at the Fermi level and a large magnetoresistance effect [135]. This is demonstrated by XMCD–PEEM imaging at the Co and Fe L_3-edges (Fig. 26). Dark and bright areas represent the induced micron-sized domains with magnetization opposite and parallel to the projection of the photon respectively. The similarity in the contrast of the Co and Fe images demonstrates ferromagnetic coupling, for antiferromagnetic coupling the images would be inverted.

For the study of multilayered magnetic materials, XMCD can be coupled with depth-resolving techniques to resolve magnetic structure beneath the surface. These use, for example, X-ray standing waves [136] or alternatively exploit the narrow escape depth of the photoelectron (Fig. 27) [137]. This latter approach has been applied to ultra-thin films of Fe grown on Cu(1 0 0), allowing the magnetic moment of individual layers to be determined. In case of a 4 multilayer (ML) film, the XMCD for each of the layers were essentially identical (Fig. 27). On the other hand, the XMCD signal for the top 2 layers of a 8 ML film (Fig. 27) shows significant dichroism, while the inner 6 layers showed little XMCD [137]. This shows that while the 4 ML films is uniformly magnetized, the surface region of the 8 ML film is ferromagnetically coupled while the inner region does not possess any average magnetization.
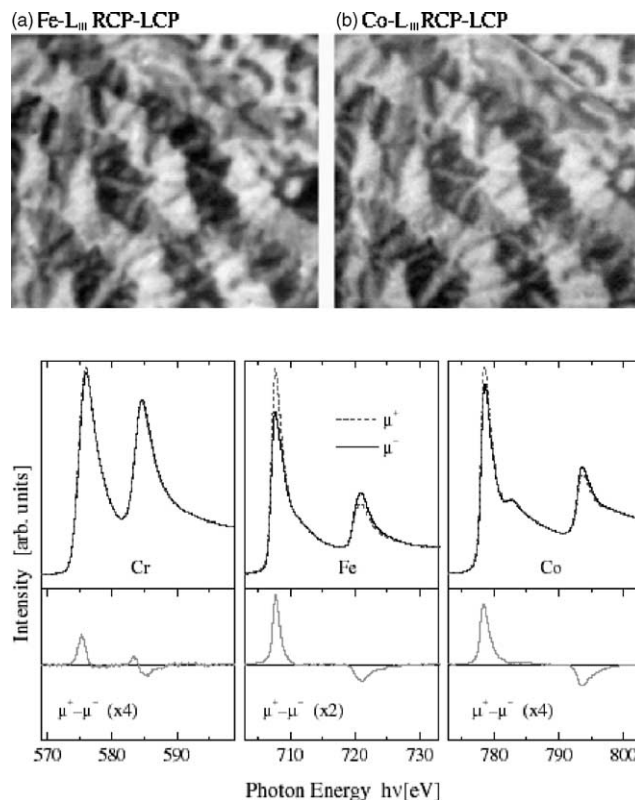

Fig. 26. (Left) XMCD–PEEM images over $9.3 \times 8.3\,\mu m^2$ region using (a) Fe and (b) Co L_3-edges. These illustrate the micromagnetic domains that are prevalent in $Co_2Cr_{0.6}Fe_{0.4}Al$. Magnetic domains that are opposite or parallel to the direction of the photon beam appear dark and light respectively. (Right) The upper and the lower panel show the Cr Fe and Co 2p XAS and MCD spectra are shown for the quenched $Co_2Cr_{0.6}Fe_{0.4}Al$ system. Reprinted with permission from [135]. Copyright (2003), Institute of Physics.
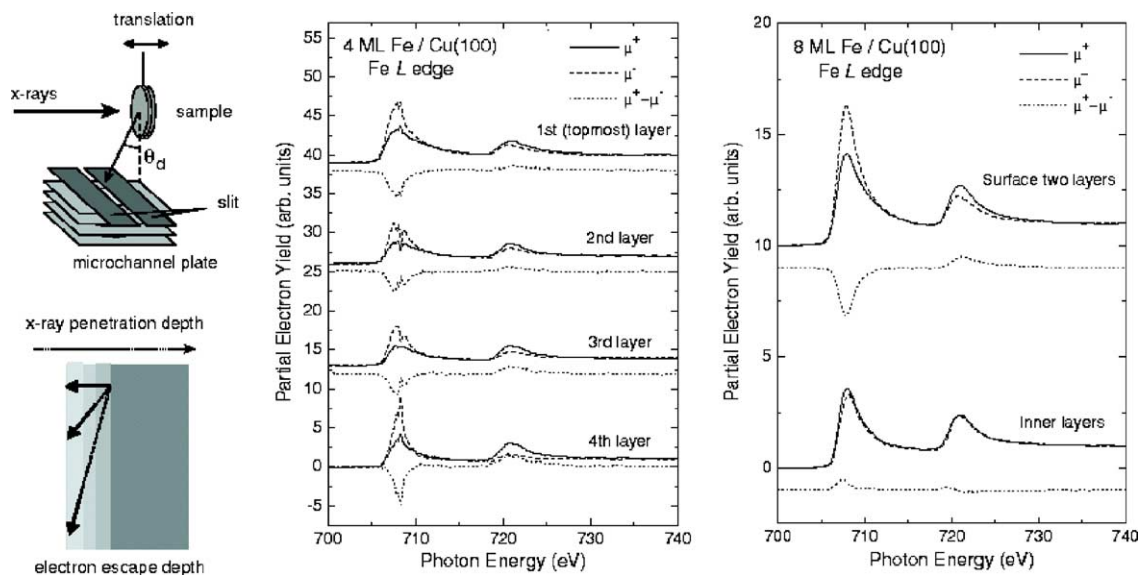
Fig. 27. (Left) Schematic diagram of depth-resolved XMCD measurements of magnetic multilayers. By moving the sample along the incident beam axis, the electron detection angle θ_d can be altered, thus decreasing the electron escape depth. Spectra were measured at 110 K; samples were magnetized prior to measurement. (Center) Fe L-edge absorption and XMCD spectra for each layer of a 4 ML Fe film. (Right) Fe L-edge absorption and XMD spectra (dotted line) for surface two layers and inner six-layer thick region for a 8 ML Fe film. Reprinted with permission from [137]. Copyright (2003), Institute of Physics.

4.7. Electronic structure

In UV–vis spectroscopy, MCD is often used to bring out detail in absorption spectra that are otherwise broad and featureless. L-edge XMCD can be used in the same manner. For example, the L-edge spectra of V(II) and V(III) complexes are relatively uninformative, and can be modeled by a wide set of ligand field parameters. In contrast, the XMCD spectra contain a wealth of structure that puts additional constraints on any LFMT simulation (Fig. 28).

XMCD can also help to distinguish p → d transitions from those that are primarily charge transfer in nature. In Fig. 28, we show some recent XMCD spectra for a Ni(I) complex from Charles Riordan's lab. As expected for a d^9 system,
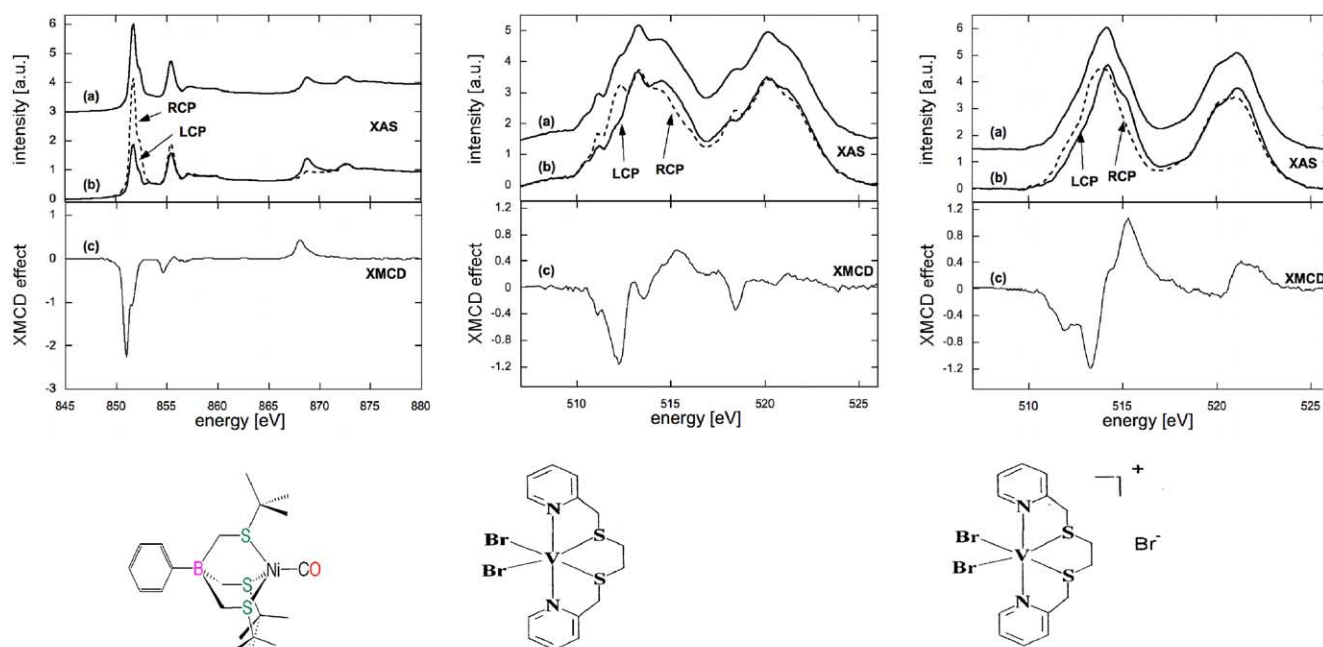

Fig. 28. (Left) Ni L-edge and XMCD for Riordan's Ni(I)CO Complex. The lower panel shows the structure and DFT calculations for this sample. (Middle and right) V L-edge and XMCD for V(II) and V(III) complexes respectively from the Rehder lab. All spectra were recorded at 2.2 K and 6 T.

there is a strong signal at the L_3-edge, and the XMCD approaches a 100% effect at the L_2-edge. In contrast, a feature near 856 eV has almost no dichroism. We attribute the latter to a charge transfer transition to an empty π^* orbital. DFT calculations are being done in collaboration with Jorge Rodrigues to quantify these assignments (Fig. 28).

5. Summary—a dose of reality

Few would argue that XMCD spectra, in principle, contain a wealth of information. As circularly polarized beamlines proliferate worldwide, access to and conduct of these measurements should become significantly easier. In ideal cases, XMCD should be able to reveal: (a) the distribution of spin and orbital angular momentum in transition metal complexes (from sum rule analysis), (b) the strength of magnetic coupling between different centers (from the field dependence), and (c) the total magnetic moment (from the magnetization curve). In practice, intelligent use of the technique requires some caution—*caveat emptor*.

For example, for systems more complicated than d^9 ions, the XMCD effect at a given edge is often bipolar or even more complex (see the calculations of van der Laan and Thole [78] and witness the detailed analysis of an Mn_{12} cluster discussed above). For the analysis of coupled systems, one is often faced with the question—is the XMCD bipolar because of antiferromagnetically coupled ions, or because of side lobes in a single component spectrum? In the extreme cases of Fe–S clusters, it seems that individual features can completely overlap, leaving a relatively featureless XMCD with multiple interpretations.

Experimental artifacts are also a concern, particularly radiation damage. Many samples are photoreduced in seconds on modern beamlines, and precautions such as sample motion or rapid scanning are often essential. Other potential problems include surface oxidation of reactive samples, beam heating at cryogenic temperatures, and surface anisotropy of magnetic properties. As discussed above, each detection scheme has the potential for mistakes as well.

Despite these potential difficulties, XMCD opens a window into electronic and magnetic structure and provides information that is often difficult to obtain by other techniques. For bioinorganic samples, it is likely that there will be considerable improvement in experimental sensitivity. This can be obtained with larger arrays of faster and/or higher resolution detectors, such as superconducting tunnel junction (STJ) detectors [138] or perhaps improved Si devices such as 'drift detectors' [139,140]. More rapid circular polarization switching will also yield better S/N in XMCD spectra. Higher field magnets will allow experiments on wider ranges of nested magnetization curves, while faster B field scans will yield more precise magnetization curves. All of these improvements are underway at the ALS and other synchrotron sources. Overall, one can be optimistic about the future of this technique. XMCD is already well established

in magnetic materials science, and it is likely to become a significant tool for the inorganic and bioinorganic communities.

References

[1] J. Stöhr, J. Electron Spectrosc. Relat. Phenom. 75 (1995) 253.
[2] P. Zeeman, Nobel Lecture, 1902.
[3] M. Born, E. Wolf, Principles of Optics, fifth ed., Macmillan, New York, 1974.
[4] R.A. Beth, Phys. Rev. 50 (1936) 115.
[5] R.P. Feynman, R.B. Leighton, M. Sands, The Feynman Lectures on Physics, vol. 1, Addison-Wesley, Reading, 1963.
[6] D.S. Kliger, J.W. Lewis, C.E. Randall, Polarized Light in Optics and Spectroscopy, Academic Press, San Diego, 1990.
[7] C. Huygens, Traité de la lumière Leiden, 1690.
[8] É.L. Maulus, Bul. Sci. Soc. Philos. (1809) 1.
[9] I. Newton, Opticks: Or, a Treatise of the Reflexions, Refractions, Inflexions and Colours of Light, S. Smith and B. Walford, London, 1704.
[10] A. Fresnel, Oeuvres Completes, Imprimerie Imperiale, Paris, 1866.
[11] M. Faraday, Experimental Research, vol. 3, London, 1855.
[12] M. Faraday, Experimental Researches in Electricity, Green Lion Press, 2000.
[13] J.C. Maxwell, A Treatise on Electricity and Magnetism, Oxford, 1873.
[14] P. Zeeman, Nature 55 (1897) 347.
[15] W.C. Röntgen, Nature 53 (1896) 274.
[16] A.H. Forman, Phys. Rev. 3 (1914) 306.
[17] A.H. Forman, Phys. Rev. 7 (1916) 119.
[18] J.L. Erskine, E.A. Stern, Phys. Rev. B 12 (1975) 5016.
[19] E. Keller, E.A. Stern, in: K.O. Hodgson, B. Hedman, J.E. Penner-Hahn (Eds.), EXAFS and Near Edge Structure III, Springer, Berlin, 1984, p. 507.

[20] B.T. Thole, G. van der Laan, G.A. Swatazky, Phys. Rev. Lett. 55 (1985) 2086.

[21] G. van der Laan, B.T. Thole, G.A. Sawatzky, J.B. Goedkoop, J.C. Fuggle, J.-M. Esteva, R. Karnatak, J.P. Remeika, H.A. Dabkowska, Phys. Rev. 34 (1986) 6529.

[22] G. Schütz, W. Wagner, W. Wilhelm, P. Kienle, R. Zeller, R. Frahm, G. Materlik, Phys. Rev. Lett. 58 (1987) 737.

[23] C.T. Chen, F. Sette, Y.-J. Ma, S. Modesti, Phys. Rev. B 42 (1990) 7262.

[24] J. van Elp, S.J. George, J. Chen, G. Peng, C.T. Chen, L.H. Tjeng, G. Meigs, H.J. Lin, Z.H. Zhou, M.W.W. Adams, B.G. Searle, S.P. Cramer, Proc. Natl. Acad. Sci. U.S.A. 90 (1993) 9664.

[25] E. Goering, J. Will, J. Geissler, M. Justen, F. Weigand, G. Schuetz, J. Alloys Compd. 328 (2001) 14.

[26] J.A.M. Cox, Ph.D. Thesis, University of Leiden, 1954.

[27] W.J. Huiskamp, Ph.D. Thesis, University of Leiden, 1958.

[28] S.P. Reynolds, Space Sci. Rev. 99 (2001) 177.

[29] M. Hart, Philos. Magn. B 38 (1978) 41.

[30] P. Scalicky, C. Malgrange, Acta Crystallogr. A 28 (1972) 501.

[31] K.-J. Kim, SPIE Proc. 1548 (1991) 73.

[32] J. Goulon, P. Elleaume, D. Raoux, Nucl. Instrum. Methods Phys. Res. A 254 (1987) 192.

[33] D. Lefebvre, P. Sainctavit, C. Malgrange, Rev. Sci. Instrum. (1994) 65.

[34] S. Yamamoto, H. Kitamura, Japan J. App. Phys. 2, 26 (1987) L1613.

[35] K.-J. Kim, SPIE Proc. 1345 (1991) 116.

[36] H. Kitamura, Syn. Rad. News 5 (1992) 14.

[37] A.T. Young, V. Martynov, H. Padmore, J. Electron Spectrosc. Relat. Phenom. 103 (1999) 885.

[38] J.A. Golovchenko, B.M. Kincaid, R.A. Levesque, A.E. Meixner, D.R. Kaplan, Phys. Rev. Lett. 57 (1986) 202.

[39] D.M. Mills, Nucl. Inst. Methods A 266 (1988) 531.

[40] D.M. Mills, in: D.M. Mills (Ed.), Third Generation Hard X-Ray Synchrotron Radiation Sources: Source Properties, Optics, and Experimental Techniques, John Wiley & Sons, New York, 2002, p. 41.

[41] C. Giles, C. Malgrange, J. Goulon, F. Debergevin, C. Vettier, A. Fontaine, E. Dartyge, S. Pizzini, F. Baudelet, A. Freund, Rev. Sci. Instrum. 66 (1995) 1549.

[42] L.C.G. Varga, Y.L. Zheng, S. Pizzini, F. de Bergevin, A. Fontaine, C. Malgrange, J. Syn. Rad. 6 (1999) 1125.

[43] W. Leitenberger, C. Eisenschmidt, H.-R. Höche, J. Appl. Crystallogr. 30 (1997) 164.

[44] J.W. Freeland, J.C. Lang, G. Srajer, R. Winarksi, D. Shu, D.M. Mills, Rev. Sci. Instrum. 73 (2002) 1408.

[45] J. Stöhr, Y. Wu, B.D. Hermsmeier, M.G. Samant, G.R. Harp, S. Koranda, D. Dunham, B.P. Tonner, Science 259 (1993) 658.

[46] J.G. Tobin, G.D. Waddill, A.F. Jankowski, P.A. Sterne, D.P. Pappas, Phys. Rev. B 52 (1995) 6530.

[47] H.A. Dürr, G. van der Laan, D. Spanke, F.U. Hillebrecht, N.B. Brookes, Phys. Rev. B 56 (1997) 8156.

[48] R. Nakajima, Ph.D. Thesis, Stanford University, 1997.

[49] S.J. George, J. van Elp, J. Chen, S. Mitra-Kirtley, O.C. Mullins, S.P. Cramer, in: B. Chance (Ed.), Synchrotron Radiation in Biosciences, Oxford University Press, Oxford, 1994.

[50] J. Christiansen, G. Peng, A.T. Young, L.B. LaCroix, E.I. Solomon, S.P. Cramer, Inorg. Chim. Acta 118 (1996) 229.

[51] C. Bryant, M.S. Thesis, University of California, Davis, 1998.

[52] P.A. Lee, P.H. Citrin, P. Eisenberger, B.M. Kincaid, Rev. Mod. Phys. 53 (1981) 769.

[53] C.T. Chen, Y.U. Idzerda, H.J. Lin, N.V. Smith, G. Meigs, E. Chaban, G. Ho, E. Pellegrin, F. Sette, Phys. Rev. Lett. 75 (1995) 152.

[54] E.A. Stern, K. Kim, Phys. Rev. B 23 (1981) 3781.

[55] J. Goulon, C. Goulon-Ginet, R. Cortes, J.M. Dubois, J. Phys. 43 (1982) 539.

[56] J. Stöhr, R. Nakajima, IBM J. Res. Dev. 42 (1998) 73.

[57] F.M.F. de Groot, M.-A. Arrio, P. Sainctavit, C. Cartier, C.T. Chen, Solid State Commun. 92 (1994) 991.

[58] F.M.F. de Groot, M.-A. Arrio, P.C.C. Sainctavit, C.T. Chen, Physica B 208–209 (1995) 84.

[59] M. Pompa, A.M. Flank, P. Lagarde, J.C. Rife, I. Stekhin, M. Nakazawa, H. Ogasawara, A. Kotani, Phys. Rev. B 56 (1997) 2267.

[60] M.M. van Veenendaal, J.B. Goedkoop, B.T. Thole, Phys. Rev. Lett. 77 (1996) 1508.

[61] J.B. Goedkoop, N.B. Brookes, M. van Veenendaal, B.T. Thole, J. Electron Spectrosc. Relat. Phenom. 86 (1997) 143.

[62] P. Carra, R. Benoist, Phys. Rev. B 62 (2000) R7703.

[63] R.D. Peacock, B. Stewart, J. Phys. Chem. B 105 (2001) 351.

[64] J. Stöhr, Y. Wu, in: A.S. Schlacter, F.J. Wuilleumier (Eds.), New Directions in Research with Third-Generation Soft X-Ray Synchrotron Radiation Sources, Kluwer, Amsterdam, 1994, p. 221.

[65] H.A. Bethe, E.E. Salpeter, Quantum Mechanics of One- and Two-Electron Atoms, Plenum Press, New York, 1977.

[66] L.H. Tjeng, B. Sinkovic, N.B. Brookes, J.B. Goedkoop, R. Hesper, E. Pellegrin, F.M.F. deGroot, S. Altieri, S.L. Hulbert, E. Shekel, G.A. Sawatzky, Phys. Rev. Lett. 78 (1997) 1126.

[67] N.B. Brookes, B. Sinkovic, L.H. Tjeng, J.B. Goedkoop, R. Hesper, E. Pellegrin, F.M.F. de Groot, S. Altieri, S.L. Hulbert, E. Shekel, G.A. Sawatzky, J. Electron Spectrosc. Relat. Phenom. 92 (1998) 11.

[68] G. Schütz, P. Fischer, E. Goering, K. Attenkofer, D. Ahlers, W. Rößl, Syn. Rad. News 10 (1997) 13.

[69] C. Brouder, M. Hikam, Phys. Rev. B 43 (1991) 3809.

[70] A.I. Nesvizhskii, A.L. Ankudinov, J.J. Rehr, K. Baberschke, Phys. Rev. B 62 (2000) 15295.

[71] T. Jo, G.A. Sawatzky, Phys. Rev. B 43 (1991) 8771.

[72] G. Vanderlaan, B.T. Thole, J. Phys. Condes. Matter 4 (1992) 4181.

[73] T. Yamaguchi, S. Shibuya, S. Suga, S. Shin, J. Phys. C 15 (1982) 2641.

[74] B.T. Thole, G. van der Laan, P.H. Butler, Chem. Phys. Lett. 149 (1988) 295.

[75] G. van der Laan, B.T. Thole, G.A. Sawatzky, M. Verdaguer, Phys. Rev. B 37 (1988) 6587.

[76] F.M.F. de Groot, J.C. Fuggle, B.T. Thole, G.A. Sawatzky, Phys. Rev. B 41 (1990) 928.

[77] F.M.F. de Groot, J.C. Fuggle, B.T. Thole, G.A. Sawatzky, Phys. Rev. B 42 (1990) 5459.

[78] G. van der Laan, B.T. Thole, Phys. Rev. B 43 (1991) 13401.

[79] G. van der Laan, B.T. Thole, Phys. Rev. B 42 (1990) 6670.

[80] M. Weissbluth, Atoms and Molecules, Plenum Press, New York, 1978.

[81] P.H. Butler, Point Group Symmetry. Applications, Methods and Tables, Plenum Press, New York, 1981.

[82] R.D. Cowan, The Theory of Atomic Structure and Spectra, University of California Press, Berkeley, 1981.

[83] F.A. Cotton, Chemical Applications of Group Theory, third ed., Wiley-Interscience, New York, 1990.

[84] F.M.F. de Groot, Chem. Rev. 101 (2001) 1779.

[85] G. van der Laan, J. Phys. Soc. Jpn. 63 (1994) 2393.

[86] J. van Elp, B.G. Searle, J. Electron. Spectrosc. Relat. Phenom., 1997.

[87] B.T. Thole, P. Carra, F. Sette, G. van der Laan, Phys. Rev. Lett. 68 (1992) 1943.

[88] P. Carra, B.T. Thole, M. Altarelli, X.D. Wang, Phys. Rev. Lett. 70 (1993) 694.

[89] P.W. Atkins, R.S. Friedman, Molecular Quantum Mechanics, third ed., Oxford University Press, Oxford, 1997.

[90] A.F. Starace, Phys. Rev. B 5 (1972) 1773.

[91] S.J. George, M.D. Lowery, E.I. Solomon, S.P. Cramer, J. Am. Chem. Soc. 115 (1993) 2968.

[92] H. Wang, P. Ge, C.G. Riordan, S. Brooker, C.G. Woomer, T. Collins, C. Melendres, O. Graudejus, N. Bartlett, S.P. Cramer, J. Phys. Chem. B 102 (1998) 8343.

[93] J. Stöhr, H. Konig, Phys. Rev. Lett. 75 (1995) 3748.

[94] P. Carra, Syn. Rad. News 5 (1992) 21.

[95] R.Q. Wu, D. Wang, A. Freeman, J. Phys. Rev. Lett. 71 (1993) 3581.

[96] R.Q. Wu, A. Freeman, J. Phys. Rev. Lett. 73 (1994) 1994.

[97] P. Sainctavit, M.A. Arrio, C. Brouder, Phys. Rev. B 52 (1995) 12766.

[98] J.T. Crocombette, B.T. Thole, F. Jollett, J. Phys. Condens. Matter 8 (1996) 4095.

[99] J.M. Moratal, A. Romero, J. Salgado, A. Perales-Alarcón, H.R. Jiménez, Eur. J. Biochem. 228 (1995) 653.

[100] H.R. Jiménez, J. Salgado, J.M. Moratal, I. Morgenstern-Badarau, Inorg. Chem. 35 (1996) 2737.

[101] T. Funk, P. Kennepohl, W.A. Wehbi, A.J. Di Bilio, A.T. Young, S. Friedrich, E. Arenholz, H.B. Gray, S.P. Cramer, J. Am. Chem. Soc. 126 (2004) 5859.

[102] D.C. Rees, Ann. Rev. Biochem. 71 (2002) 221.

[103] C.L. Drennan, J.W. Peters, Curr. Opin. Struct. Biol. 13 (2003) 220.

[104] J. van Elp, G. Peng, Z.H. Zhou, M.W.W. Adams, N. Baidya, P.K. Mascharak, S.P. Cramer, Inorg. Chem. 34 (1995) 2501.

[105] C.Y. Ralston, H. Wang, S.W. Ragsdale, M. Kumar, N.J. Spangler, P.W. Ludden, W. Gu, R.M. Jones, D.S. Patil, S.P. Cramer, J. Am. Chem. Soc. 122 (2000) 10553.

[106] T. Funk, W.W. Gu, S. Friedrich, H.X. Wang, S. Gencic, D.A. Grahame, S.P. Cramer, J. Am. Chem. Soc. 126 (2004) 88.

[107] M. Mizumaki, K. Yano, I. Umehara, K. Sato, A. Koizumi, N. Sakai, T. Muro, Phys. Rev. B 67 (2003) 132401.

[108] J. Chaboy, L.M. Garcia, F. Bartolome, H. Maruyama, S. Uemura, N. Kawamura, A.S. Markosayan, J. Appl. Phys. 88 (2000) 336.

[109] J. Chaboy, C. Piquer, N. Plugaru, M. Artigas, H. Maruyama, N. Kawamura, M. Suzuki, J. App. Phys. 93 (2003) 475.

[110] T. Honma, N. Kawamura, M. Suzuki, M. Mizumaki, H. Maruyama, N. Ishimatsu, Y. Inada, Y. Onuki, J. Phys. Condens. Matter 15 (2003) S2171.

[111] L.P. Regnault, W.A.C. Erkelens, J. Rossat-Mignod, P. Lejay, J. Phys. Rev. B 38 (1988) 4481.

[112] K. Sato, Y. Ueji, K. Okitsu, T. Matsushita, Y. Amemiya, J. Syn. Rad. 8 (2001) 1021.

[113] A.V. Soldatov, T.S. Ivanchenko, S.D. Longa, A. Kotani, Y. Iwamoto, A. Bianconi, Phys. Rev. B 50 (1994) 5074.

[114] D.A. Grahame, E. Demoll, J. Biol. Chem. 271 (1996) 8352.

[115] T.I. Doukov, T.M. Iverson, J. Seravelli, S.W. Ragsdale, C.L. Drennan, Science 298 (2002) 567.

[116] C. Darnault, A. Volbeda, E.J. Kim, P. Legrand, X. Vernéede, P.A. Lindahl, J.C. Fontecilla-Camps, Nature Struct. Biol. 10 (2004) 271.

[117] J. Seravalli, Y. Xiao, W. Gu, S.P. Cramer, W.E. Antholine, V. Krymov, G.J. Gerfen, S.W. Ragsdale, Biochemistry 43 (2004) 3944.

[118] H. Wang, C.Y. Ralston, D.S. Patil, R.M. Jones, W. Gu, M. Verhagen, M.W.W. Adams, P. Ge, C. Riordan, C.A. Marganian, P. Mascharak, J. Kovacs, C.G. Miller, T.J. Collins, S. Brooker, P.D. Croucher, K.

[119] Wang, E.I. Stiefel, S.P. Cramer, J. Am. Chem. Soc. 122 (2000) 10544.

[119] P. Rudolf, F. Sette, L.H. Tjeng, G. Meigs, C.T. Chen, J. Magn. Magn. Mater. 109 (1992) 109.

[120] D.C. Rees, J.B. Howard, Curr. Opib. Struct. Biol. 4 (2000) 559.

[121] J. Barber, J.M. Anderson, Philos. Trans. R. Soc. Lond. B 357 (2002) 1325.

[122] R. Sessoli, H.-L. Tsai, A.R. Schake, S. Wang, J.B. Vincent, K. Folting, D. Gatteschi, G. Christou, D.N. Hendrickson, J. Am. Chem. Soc. 115 (1993) 1804.

[123] R. Moroni, C.C.D. Moulin, G. Champion, M.-A. Arrio, P. Sainctavit, M. Verdaguer, D. Gatteschi, Phys. Rev. B 68 (2003) 064401.

[124] P. Ghigna, A. Campana, A. Lascialfari, A. Caneschi, D. Gatteschi, A. Tagliaferri, F. Borgatti, Phys. Rev. B 64 (2001) 132413.

[125] Y. Ayant, E. Belorizk, M. Guillot, J. Rosset, J. de. Phys. 26 (1965) 385.

[126] G. Peng, J. van Elp, H. Jang, L. Que, W.H. Armstrong, S.P. Cramer, J. Am. Chem. Soc. 117 (1995) 2515.

[127] J. van Elp, G. Peng, Z.H. Zhou, S. Mukund, M.W.W. Adams, Phys. Rev. B 53 (1996) 2523.

[128] A. Deb, M. Mizumaki, T. Muro, Y. Sakurai, V. Tsurkan, Phys. Rev. B 68 (2003) 014421.

[129] H. Wang, C. Bryant, D.W. Randall, L.B. LaCroix, E.I. Solomon, M. LeGros, S.P. Cramer, J. Phys. Chem. B 102 (1998) 8347.

[130] C.H.F.R.E. Tsang Jr., T. Lin, D.E. Helm, B.A. Gurney, M.L. Williams, IBM J. Res. Dev. 42 (1998) 103.

[131] B.D. Cullity, Introduction to Magnetic Materials, Addison-Wesley, Reading, MA, 1972.

[132] M. Bonfim, G. Ghiringhelli, F. Montaigne, S. Pizzini, N.B. Brookes, F. Petroff, J. Vogel, J. Camarero, A. Fontaine, Phys. Rev. Lett. 86 (2001) 3646.

[133] E.G. Pavel, E.I. Solomon, in: E.I. Solomon, K.O. Hodgson (Eds.), Spectroscopic Methods in Bioinorganic Chemistry, vol. 692, American Chemical Society, Washington, DC, 1998, p. 119.

[134] J. Stöhr, H.A. Pademore, S. Anders, T. Stammler, M.R. Scheinfein, Surf. Rev. Lett. 5 (1998) 1297.

[135] C. Felser, B. Heitkamp, F. Kronast, D. Schmitz, S. Cramm, H.A. Durr, H.J. Elmers, G.H. Fecher, S. Wurmehl, T. Block, D. Valdaistev, S.A. Nepijko, A. Gloskovskii, G. Jakob, G. Schonhense, W. Eberhardt, J. Phys. Condens. Matter 15 (2003) 7019.

[136] S.-K. Kim, J.B. Kortright, 86 (2001) 1347.

[137] K. Amemiya, S. Kitagawa, D. Matsumara, T. Yokoyama, T. Ohta, J. Phys. Condens. Matter 15 (2003) S561.

[138] S. Friedrich, T. Funk, O.S.E. Drury, S.P. Labov, S.P. Cramer, Rev. Sci. Inst. 73 (2002) 1629.

[139] E. Gatti, P. Rehak, Nucl. Instrum. Methods A 225 (1984) 608.

[140] L. Strüder, P. Lechner, P. Leutenegger, Naturwiss 85 (1998) 539.